Geochemistry, Geophysics, Geosystems®

AGU ADVANCING EARTH AND SPACE SCIENCE

RESEARCH ARTICLE
10.1029/2022GC010794

**Key Points:**

- >700 fissures mapped at 1-m bathymetric resolution at 9°50′N East Pacific Rise, most of which were active during the 2005–2006 eruptions
- Fault slip and crack opening accommodate <0.3% of plate separation, indicating the dominant role of diking at fast-spreading ridges
- Fissures and lava flow located >2 km from the ridge axis are spatially associated with off-axis lower crustal off-axis magma lens

**Supporting Information:**

Supporting Information may be found in the online version of this article.

**Correspondence to:**

J.-N. Wu,
wjyunnai@ucsd.edu

**Citation:**

Wu, J.-N., Parnell-Turner, R., Fornari, D. J., Berrios-Rivera, N., Barreyre, T., & McDermott, J. M. (2023). The Role of On- and Off-axis Faults and Fissures during Eruption Cycles and Crustal Accretion at 9°50′N, East Pacific Rise. *Geochemistry, Geophysics, Geosystems*, *24*, e2022GC010794. https://doi.org/10.1029/2022GC010794

Received 23 NOV 2022
Accepted 1 APR 2023

**Author Contributions:**

**Conceptualization:** Jyun-Nai Wu, Ross Parnell-Turner
**Data curation:** Jyun-Nai Wu, Daniel J. Fornari, Natalia Berrios-Rivera
**Formal analysis:** Jyun-Nai Wu
**Funding acquisition:** Ross Parnell-Turner, Daniel J. Fornari, Thibaut Barreyre, Jill M. McDermott
**Investigation:** Jyun-Nai Wu, Natalia Berrios-Rivera
**Methodology:** Jyun-Nai Wu
**Project Administration:** Ross Parnell-Turner



# The Role of On- and Off-Axis Faults and Fissures During Eruption Cycles and Crustal Accretion at 9°50′N, East Pacific Rise

**Jyun-Nai Wu[1], Ross Parnell-Turner[1], Daniel J. Fornari[2], Natalia Berrios-Rivera[1], Thibaut Barreyre[3], and Jill M. McDermott[4]**

[1]Institute of Geophysics and Planetary Physics, Scripps Institution of Oceanography, University of California, San Diego, La Jolla, CA, USA, [2]Department of Geology and Geophysics, Woods Hole Oceanographic Institution, Woods Hole, MA, USA, [3]Department of Earth Science, University of Bergen, Bergen, Norway, [4]Department of Earth and Environmental Science, Lehigh University, Bethlehem, PA, USA

**Abstract** Fissures and faults provide insight into how plate separation is accommodated by magmatism and brittle deformation during crustal accretion. Although fissure and fault geometry can be used to quantify the spreading process at mid-ocean ridges, accurate measurements are rare due to insufficiently detailed mapping data. Here, fissures and faults at the fast-spreading 9°50′N segment of the East Pacific Rise were mapped using bathymetric data collected at 1-m horizontal resolution by autonomous underwater vehicle *Sentry*. Fault dip estimates from the bathymetric data were calibrated using co-registered near-bottom imagery and depth transects acquired by remotely operated vehicle *Jason*. Fissures are classified as either eruptive or non-eruptive (i.e., cracks). Tectonic strain estimated from corrected fault heaves suggests that faulting plays a negligible role in the plate separation on crust younger than 72 kyr (<4 km from the ridge axis). Pre- and post-eruption surveys show that most fissures were reactivated during the eruptions in 2005–2006. Variable eruptive fissure geometry could be explained by the frequency with which each fissure is reactivated and partially infilled. Fissure swarms and lava plateaus in low-relief areas >2 km from the ridge are spatially associated with off-axis lower-crustal magma lenses identified in multichannel seismic data. Deep, closely spaced fissures overlie a relatively shallow portion of the axial magma lens. The width of on-axis fissures and inferred subsurface dike geometry imply a ∼9-year long diking recurrence interval to fully accommodate plate spreading, which is broadly consistent with cycle intervals obtained from estimates of melt extraction rates, eruption volumes, and spreading rate.

**Plain Language Summary** New oceanic crust is created by seafloor spreading at mid-ocean ridges, where lava erupts as the tectonic plates spread apart. Plate separation is accommodated by a combination of slip along dipping faults and the opening of magma-filled cracks, called dikes. We present bathymetric and profile mapping data collected from near the seafloor on a volcanically active portion of the East Pacific Rise near 9°50′N. The data show faults and fissures (i.e., open cracks) in remarkable detail, with meter-scale resolution. A total of 707 fissures and 42 faults were identified and measured, suggesting that the amount of plate separation accommodated by faulting is minimal compared to that by dike intrusion causing open cracks. About one-third of the fissures mapped are located within the region covered by the most recent eruptions in 2005–2006, and most of these fissures seem to have been reactivated from previous eruptions. Based on measurements of fissure width, we estimate that the interval between diking events is ∼9 years, which agrees with previous independent estimates. The analysis in this study reveals the relative importance of faults and fissures in seafloor spreading, and in the magmatic cycles that continuously re-pave the ocean floor.

## 1. Introduction

Seafloor spreading at mid-ocean ridges (MORs) is accommodated by a combination of faulting and magmatism (Buck et al., 2005; Kappel & Ryan, 1986; Luyendyk, 1970; Macdonald et al., 1996; T. J. Wright et al., 2012). Partitioning of seafloor spreading between slip on faults and magmatic diking varies considerably, and is thought to be partly controlled by spreading rate (e.g., Buck et al., 2005; Cowie et al., 1993; Ito & Behn, 2008; Olive & Dublanchet, 2020). At most fast-spreading MORs (full rate ∼>10 cm/yr), the proportion of plate separation accommodated by magmatism, $M$, is estimated to exceed 0.9, that is, less than 10% of plate separation is accommodated by slip on faults. At slow spreading MORs (full rate ∼<2 cm/yr), $M$ can be highly variable (∼0.2–0.6;

**Resources:** Jyun-Nai Wu
**Software:** Jyun-Nai Wu
**Supervision:** Ross Parnell-Turner
**Validation:** Jyun-Nai Wu
**Visualization:** Jyun-Nai Wu
**Writing – original draft:** Jyun-Nai Wu
**Writing – review & editing:** Jyun-Nai Wu, Ross Parnell-Turner, Daniel J. Fornari, Thibaut Barreyre, Jill M. McDermott

e.g., Ito & Behn, 2008; Olive & Dublanchet, 2020). Magma supply is a key factor controlling faulting style, in which an increase in $M$ usually results in a decrease in fault heave and fault spacing (Behn & Ito, 2008; Buck et al., 2005). Despite the importance of $M$, quantifying the amount of magmatic accretion at a given site is challenging. One common way to estimate the partitioning of plate separation along MORs is to estimate the tectonic extension, $T$ (i.e., $1-M$) from observations of strain on fault scarps (e.g., Escartín et al., 1999, 2007; Le Saout et al., 2018, 2021). Although studies of faults and fissures have provided useful estimates of tectonic extension at MORs, they are often limited by the resolution of data, imaging artifacts, navigation uncertainty in sidescan sonar images, and the effects of volcanic repaving (e.g., Escartín et al., 2007). Furthermore, previous fault heave measurements rely on fault dip estimates which can be biased by incomplete seafloor insonification and the presence of talus at the base of fault scarps (e.g., Escartín et al., 1999).

Early pioneering estimates of tectonic strain from faulting on MORs using deep-tow sidescan sonar imagery or shipboard bathymetric data are limited by data resolution as mentioned above (e.g., Bohnenstiehl & Carbotte, 2001; Carbotte & Macdonald, 1992; Escartín et al., 1999). Recent developments in underwater navigation and mapping sonars provide opportunities for meter-resolution mapping with autonomous underwater vehicles (AUVs; Bohnenstiehl & Carbotte, 2001; Caress et al., 2012; Clague et al., 2017, 2018; Wu et al., 2022; Yoerger et al., 1998, 2007). Analysis of faults and fissures using deep-towed sidescan sonar data suggests that the tectonic strain accommodated by normal faults on fast-spreading MORs is typically less than 10% (e.g., Bohnenstiehl & Carbotte, 2001; Escartín et al., 2007). In contrast, the geometry of faults and fissures mapped using meter-resolution bathymetric data on the Juan de Fuca Ridge indicated the tectonic component of spreading to be 2–3 times larger than for other MORs with similar spreading rates (Le Saout et al., 2021). These studies suggested that resolving the geometry of individual faults and fissures with traditional approaches is limited, and that meter-scale data add important information for a more complete view of strain partitioning at MORs.

Our understanding of the formation of fissures (i.e., open cracks in the seafloor) is mostly based on numerical models and terrestrial field observations in subaerial volcanic provinces (e.g., Gudmundsson & Bäckström, 1991; Hjartardóttir, Einarsson, & Björgvinsdóttir, 2016; Hjartardóttir, Einarsson, Magnúsdóttir, et al., 2016; Hjartardóttir et al., 2012; Lundgren et al., 2013; Rubin, 1992). Fissures can be categorized as eruptive or non-eruptive structures (e.g., Hjartardóttir et al., 2009). Here, we define eruptive fissures as individual, linear features that have been sites of lava extrusion, likely sourced by deep-rooted feeder dikes formed by tension related to magma injection (Koehn et al., 2019; Rubin, 1992; Rubin & Pollard, 1988; Tentler & Temperley, 2007; T. J. Wright et al., 2006). In contrast, non-eruptive fissures are linear, tectonic features not associated with surface lava eruptions that arise due to far-field stress and are usually orientated perpendicular to the principal stress direction or *en échelon* (Chorowicz et al., 1994; Gibson, 1969; Nakamura, 1970). Earlier studies of fissures on MORs suggested that eruptive fissure length for individual eruptions might reflect the lateral connectivity of subsurface magma bodies along the axis, and therefore is proportional to spreading rate (e.g., Sinton et al., 2002). However, previous detailed fissure analyses have been restricted to a few small areas where meter-resolution data are available (e.g., Le Saout et al., 2018, 2021); hence, the relationship between the processes responsible for fissure creation and subsurface magma systems remains unclear.

## 2. The 9°50′N Study Area

The 9°–10°N segment of the East Pacific Rise (EPR) is located between the Clipperton and Siqueiros transform faults, and is one of the most intensely studied mid-ocean ridge segments (e.g., Fornari et al., 1998, 2012; Harding et al., 1993; Haymon et al., 1991, 1993; Macdonald & Fox, 1988; Orcutt et al., 1976; Tolstoy et al., 2006; D. J. Wright, Haymon, & Fornari, 1995; D. J. Wright, Haymon, & MacDonald, 1995). The EPR in this region is comprised of a broad axial high capped by a ~10–20 m-deep axial summit trough (AST, Figure 1; Carbotte & Macdonald, 1992; Fornari et al., 1998, 2004). Seismic reflection images reveal an axial magma lens (AML) along ~85% of the ridge axis along this segment, at a mean depth of 1,640 ± 300 m, while the upper AML reflector shallows ~200 m from 9°40′N to 9°54′N (Aghaei et al., 2014; Canales et al., 2012; Carbotte et al., 2013; Detrick et al., 1987; Han et al., 2014; Marjanović et al., 2014, 2018; Mutter et al., 1988; Xu et al., 2014). The AML is likely the source of magma that fed the two documented eruptions along this segment, one in 1991–1992 (Haymon et al., 1993) and most recently in 2005–2006 (e.g., Cowen et al., 2007; Soule et al., 2007; Tolstoy et al., 2006). In addition to the AML, several off-axis magma lenses have been identified both in the upper and lower crust (e.g., Aghaei et al., 2014; Canales et al., 2012).

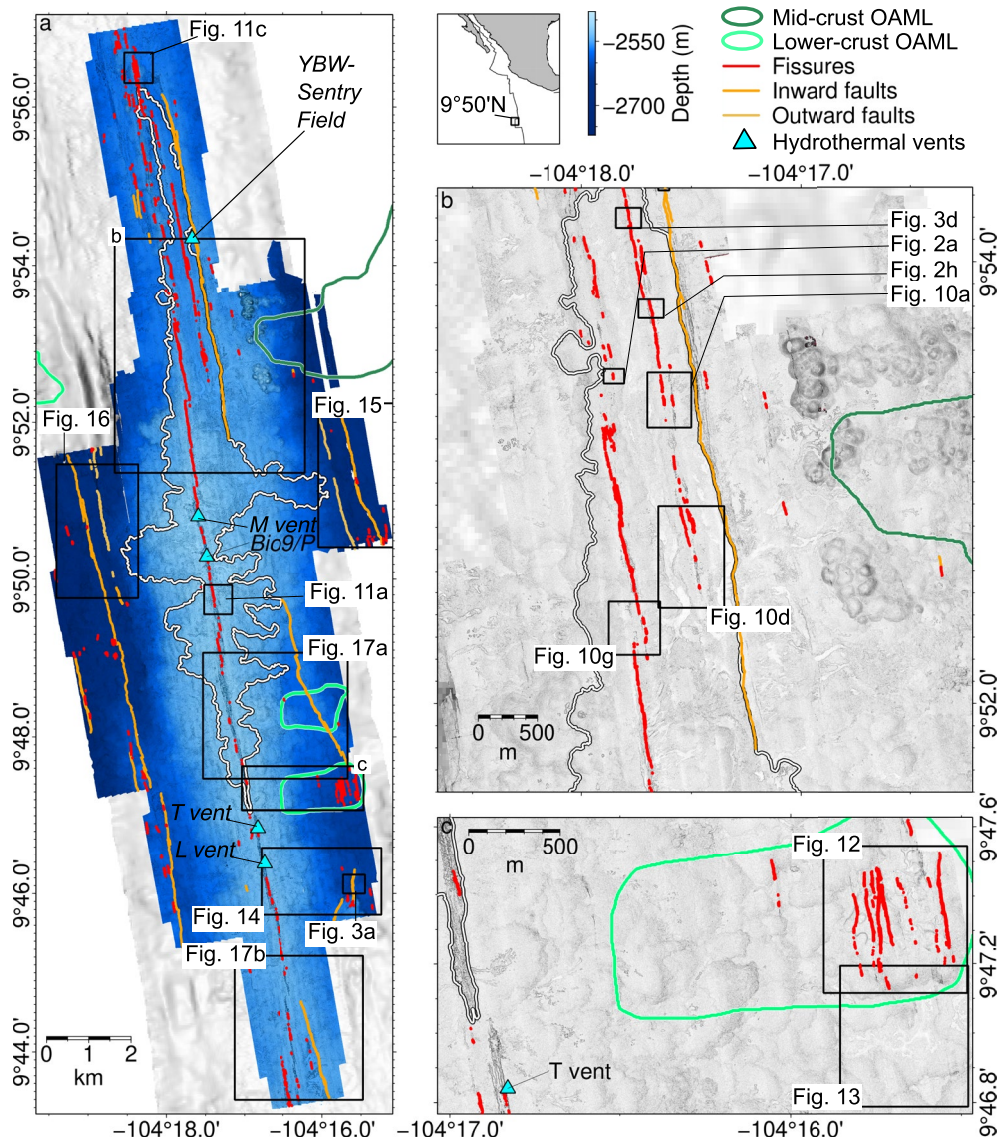


**Figure 1.** (a) 1 m-resolution bathymetric data collected with AUV *Sentry* (Wu et al., 2022); gray shaded relief is 30 m-resolution shipboard multibeam data from cruise TN188 (White et al., 2006); white outline is 2005–2006 flow extent (Wu et al., 2022); red lines are fissures; orange lines with two different shades are inward-facing and outward-facing faults; boxes show location of later figures; blue triangles show location of selected hydrothermal vents; dark green and light green polygons are off-axis magma lens (OAML; Aghaei et al., 2017). Inset: box shows study site; thin black lines are plate boundaries. (b) and (c) Shaded gray-scale bathymetry shows details of fault and fissure interpretation in the northern and southern regions of the study area shown in (a).

Previous near-bottom studies of the EPR between ~9°25′ and 55′N show that although some near-axis faults and fissures are likely buried by young lava flows, inward facing normal faults account for only about 0.7% of the total strain (Escartín et al., 2007). However, this estimated tectonic strain is uncertain due to limited meter-resolution bathymetric data coverage and lack of fissure depth information from sidescan sonar imagery.

Here, we quantify the geometry of faults and fissures identified using 1-m resolution bathymetric data collected by AUV *Sentry* in 2018–2021 over a portion of the EPR crest between 9°45′–57′N and use these data to infer tectonic strain within 4 km of the AST (Wu et al., 2022). Uncertainty in fault dip is addressed by comparing fault scarp geometry from the AUV multibeam bathymetric data with co-located near-bottom images, navigation and bathymetric profiles collected during remotely operated vehicle (ROV) *Jason* dives. The geometry and distribution of faults and fissures provide essential information for calculating improved tectonic strain estimates. Insights into the formation of fissures and their relationship to magmatic processes are gained.

## 3. Data and Methods

### 3.1. Near-Bottom Mapping Using AUV *Sentry*

Near-bottom, multibeam bathymetric data were collected with AUV *Sentry* along track lines spaced ~170 m apart at ~65 m above bottom using a Reson 7125 system in 2018, and a Kongsberg EM2040 system in 2019 and 2021. Both bathymetric systems operate at 400 kHz, while 120 kHz sidescan data were collected simultaneously with an EdgeTech 2200-M in 2018, 2019, and an EdgeTech 2205 system in 2021. Further data acquisition and processing details are given in Wu et al. (2022), who used the high-resolution bathymetric data set to map lava flows erupted in 2005–2006 over a region that extends 25.6 km along the axis and up to 8 km across-axis at its widest point near 9°50′N (Figure 1).

The 2018–2021 survey is co-located with an 8 $km^2$ near-bottom scanning altimeter bathymetric survey collected using AUV *ABE* in 2001, and with near-bottom towed DSL120a sidescan sonar data collected in 2001 (Fornari et al., 2004). These sidescan sonar images, collected before the 2005–2006 eruptions, cover the EPR from ~8°N to 10°N with ~2 m resolution. Fissures and faults identified using those data can also be found in the post-eruption 2018–2021 data set (Escartín et al., 2007; Wu et al., 2022).

Faults and fissures mapped using the compiled *Sentry* data were manually digitized by a single analyst (N. Berrios-Rivera) and reviewed by a second analyst (J.-N. Wu), who examined bathymetric depth and slope data in map view and cross-section (Figure 1). Fissures were digitized as closed polygons encircling narrow, linear bathymetric deeps with margins defined by tracing the maximum change in slope (Figure 2). The second derivative of bathymetric depth (i.e., curvature) was also used to better define sharp breaks in the slope that define the margins of fissures (Figure S1 in Supporting Information S1). Faults were digitized as polygons delineating exposed scarp surfaces, the margins of which were identified using discontinuities in bathymetric slope (Figure 3). Fault and fissure polygons were then used to extract estimates of fissure width, fissure depth, fault throw, and fault dip for each feature. Since fissures and faults are typically oriented parallel to the ridge axis with curvilinear shapes that vary along-axis, geometric parameters were extracted within each fault and fissure polygon along profiles oriented parallel to the plate spreading direction (~110°), spaced at 10 m intervals along-axis (Figure S2 in Supporting Information S1). Hence, each individual fault and fissure is associated with a population of width, depth, throw and dip measurements in the plate spreading direction.

Fissure width, $W$, is measured as the polygon width along each profile. Fissure depth, $Z_f$, is defined as the difference between the shallowest and deepest points along each profile within the polygon. Fault throw is defined as the vertical offset between the top and bottom of fault scarps, which is also the offset between the shallowest point and the deepest point as a criterion previously used to avoid underestimates (e.g., Escartín et al., 1999; Le Saout et al., 2021). Fault dip is defined as the steepest-dipping portion of the scarp along each profile to minimize underestimates due to accumulated mass wasted debris and talus (e.g., Le Saout et al., 2021).

### 3.2. Fault Dip Analysis and Correction Factor

The apparent geometry of mapped seafloor faults is biased by the resolution of the bathymetric data, which is partially controlled by survey altitude and look-angle (Escartín et al., 2007; Le Saout et al., 2021). Bathymetric resolution and fault throw are two factors controlling fault identification on high-angle slopes, such as those commonly associated with normal fault scarps (Le Saout et al., 2021). In addition to detection limits, gridded bathymetric data inevitably include some component of smoothing and interpolation, resulting in lower apparent dips.

We used co-located depth profiles acquired using ROV *Jason* to estimate uncertainty in the slope of seafloor features observed in multibeam bathymetric data from AUV *Sentry*. Both vehicles were navigated with Sonardyne AvTrak2 ultra-short baseline acoustic positioning system and navigation errors are estimated to be <2 m for the *Jason* and <5 m for the *Sentry* (Wu et al., 2022). Depth profiles were constructed by combining vehicle depth and altitude, measured with a Paroscientific pressure gauge and 1,200 kHz altimeter mounted on *Jason*. Since ROV *Jason* surveys at a relatively low altitude (<5–10 m) and low speed (<0.5 m/s), compared to the nominal 1 m resolution of profiles from AUV *Sentry* derived from ~65 m altitude and ~1–2 kt (0.5–1.0 m/s) speeds, the horizontal resolution of ROV *Jason*-derived profiles is more accurate than those based on *Sentry* data. Depth profiles used for comparison were extracted from four ROV *Jason* dives carried out during cruise RR2102 in

10.1029/2022GC010794

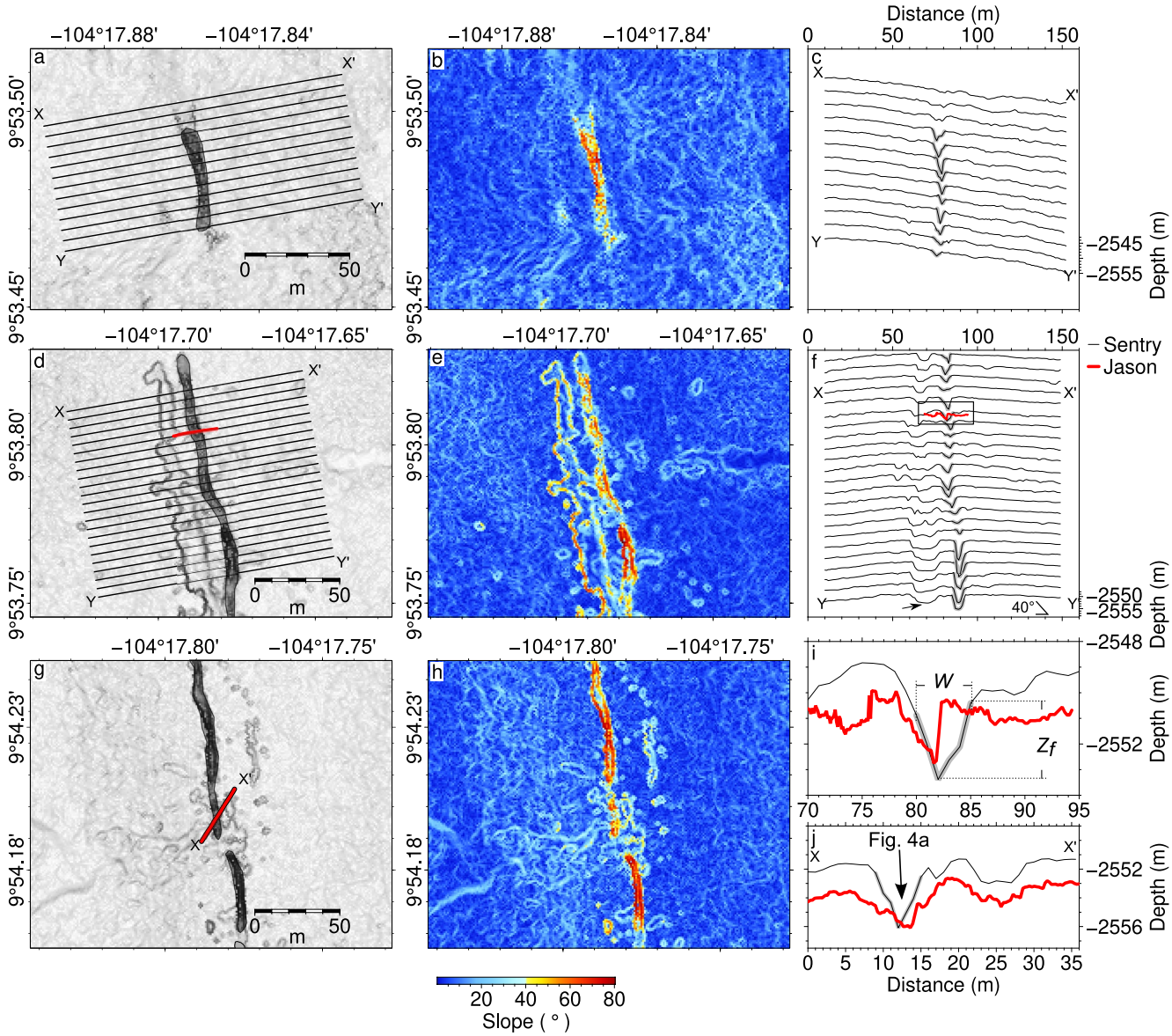


**Figure 2.** Examples of two near-axis fissures mapped using AUV *Sentry*, locations given in Figure 1. (a) Bathymetric relief over fissure near 9°53.48′N; gray shaded area is interpreted fissure; lines show locations of profiles in (c). (b) Bathymetric slope. (c) Bathymetric profiles, showing variation in fissure geometry parallel to ridge axis trend. (d–f) As above, for fissure near 9°53.78′N. Red line in (d) and (f) is depth estimated from the ROV *Jason* track; arrow in (f) is the lava channel. (g) Detailed comparison between bathymetric profile from the AUV *Sentry* (black) and depth profile estimated from the ROV *Jason* (red). Parameters of fissure width $W$ and depth $Z_f$ noted on profile. Gray bands in (c), (f), and (g) are fissures identified using multibeam bathymetric data collected by AUV *Sentry* in 2019–2021.

2021 (dives J1306, J1311, J1312, and J1322; Figure S3 in Supporting Information S1) that transited across faults, fissures, AST walls, and volcanic mounds.

Comparisons between depth profiles from ROV *Jason* and AUV *Sentry* show that the apparent dip of faults and fissures are underestimated in near-bottom multibeam sonar profiles (Figures 2g, 2j, and 3g). For example, ROV *Jason*-derived bathymetric profiles show that the normal fault located ~70 m east of the YBW-Sentry field has a staircase-like geometry with near-vertical scarps (Figure 3g). In contrast, multibeam bathymetric profiles derived from *Sentry* data imply a dip of ~75° at the same location. The vertical dip of this fault is confirmed by still and video imagery collected by ROV *Jason* (Figure 4b). To account for potential underestimates in dip from *Sentry* multibeam bathymetric data, apparent dips of seafloor features on co-registered bathymetric profiles derived from AUV *Sentry* and ROV *Jason* were examined throughout the study area (Figure 5). The dips of faults, fissures, AST walls and volcanic mounds oriented approximately perpendicular to ROV *Jason* tracklines

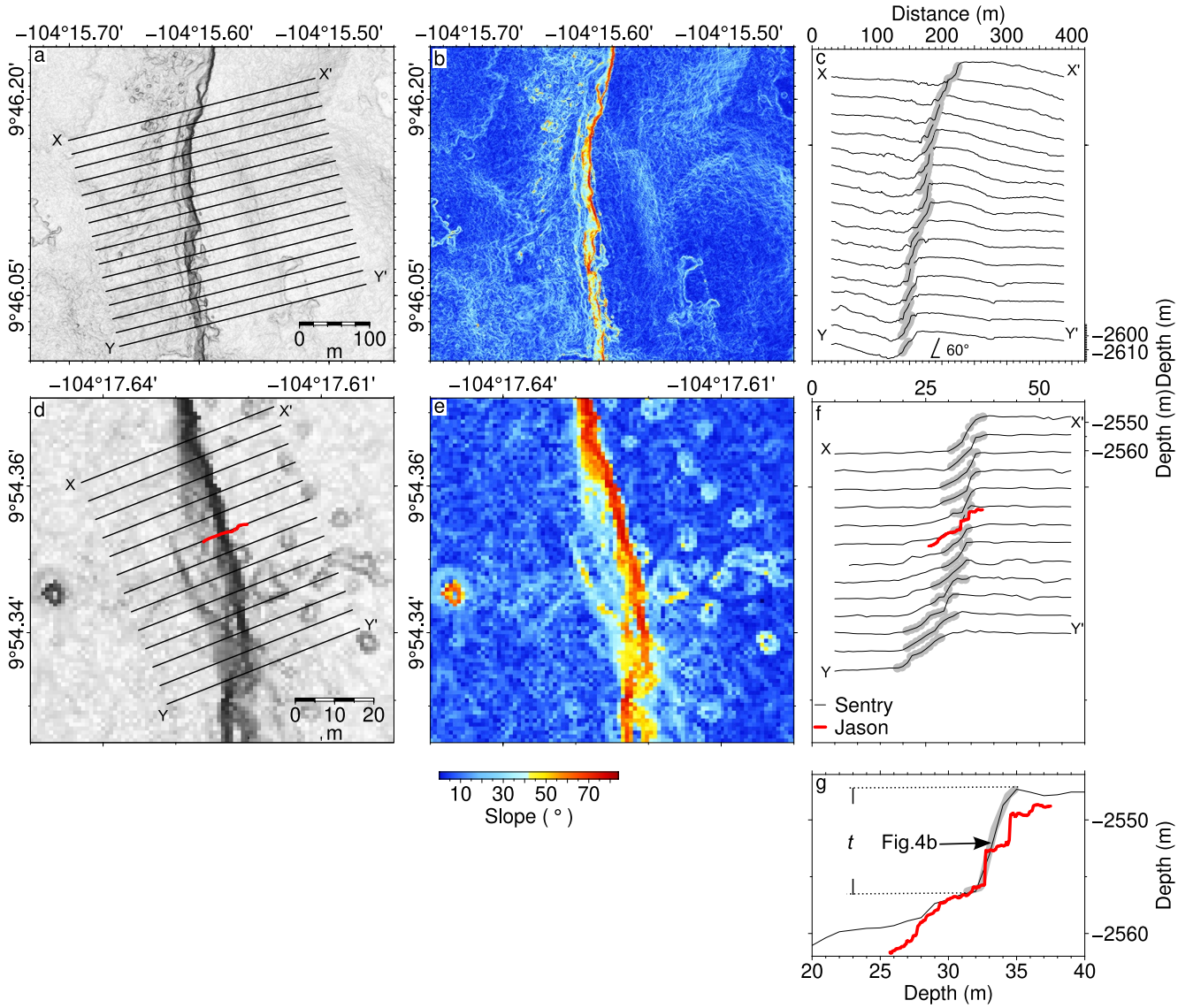


**Figure 3.** Examples of two faults mapped using the AUV *Sentry*, location given in Figure 1. (a) Bathymetric relief over the fault near 9°46′N; lines show the location of profiles in (c). (b) Bathymetric slope. (c) Bathymetric profiles showing variation in fault geometry along fault strike. (d–f) As above, for fault near 9°54.34′N. The red line in (d) and (f) is depth estimated from the ROV *Jason* track. (g) Detailed comparison between bathymetric profile from AUV *Sentry* (black), depth estimated from ROV *Jason* (red), and interpreted fault scarps (gray). Measurements of fault throw $t$ are shown on the profile. Gray bands in (c) and (f) are fault scarps identified using multibeam bathymetric data collected by AUV *Sentry* in 2019–2021.

and with vertical relief >1 m were selected for comparative analysis to minimize bias from profile orientation and navigation errors. The dip of each feature was extracted along co-located *Jason* profiles and depths extracted from gridded multibeam data from *Sentry*, and an empirical dip-dependent correction factor was obtained by fitting a second-degree polynomial function (Figure 5). We then obtain a corrected dip, $\theta_c$ using

$$\theta_c = a\theta + b\theta^2, \quad (1)$$

where $\theta$ is apparent dip measured from *Sentry* bathymetric profiles, and $a$ (1.128), and $b$ (−0.055) are coefficients that yield the best-fitting polynomial (Figure 5).

## 4. Results

Using the *Sentry* 1-m resolution multibeam data, we mapped 707 fissures, of which 381 are located within ~200 m of the ridge axis. Most fissures trend parallel to the ridge axis (~350°) and are most commonly located

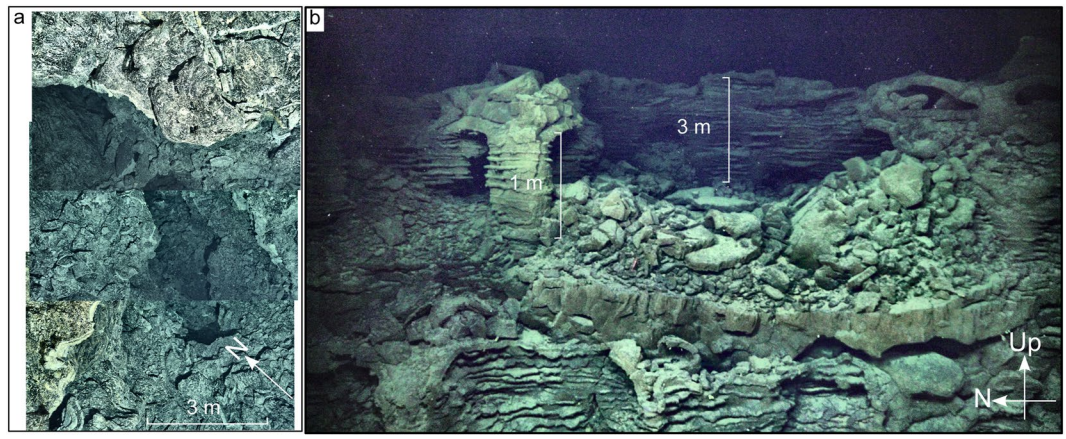


**Figure 4.** Photographic images of example fissure and fault, acquired by ROV *Jason*. (a) Three images mosaiced together over fissure located near 104°17.623′W 9°54.353′N, acquired using a down-looking 24 MP still camera during dive J1322 in April 2021; location shown in Figure 2j. (b) Still frame image from forward-looking 4K video camera during dive J1322 near 104°17.623′W 9°54.353′N, which shows an exposure of complex multi-flow internal lava structures along the fault plane. Note staircase-like fault scarp with truncated lobate flows and collapses; location shown in Figure 3g.

above or around volcanic mounds and within the AST (Figure 1). The fissures within ~200 m of ridge axis are likely to be eruptive, especially those within 2005–2006 eruption extent, while the off-axis fissures could be either eruptive or non-eruptive. We mapped a total of 42 fault scarps, of which 38 are inward facing (i.e., normal faults accommodating extension with respect to the ridge axis). Mapped faults also trend parallel to the ridge axis but are mostly located >700 m from the ridge axis and AST. Our results reveal ~two times more fissures than previously identified using near-bottom sidescan sonar data collected in 2001 and 2006, and verify the location of the previously mapped faults (Escartín et al., 2007).

### 4.1. Fissure Geometry

We extracted fissure and fault geometry parameters along 2,590 spreading-parallel profiles spaced 10 m apart (yielding a total of >6,000 individual measurements) to evaluate patterns in magmatic and tectonic morphology (Figures 6a and 6b). We find that fissure widths range from 1 to 10 m and fissure depths typically range from 1 to 6 m (Figures 6a and 6b), and that fissure width and depth are positively correlated (Figure 6e). Fissure lengths range from 3 to ~520 m (Figure 7a) and their aspect ratio (width/length) is mostly less than 0.3 (Figure 8d). In order to evaluate the tectonic extension, we consider measurements from inward facing faults (Figures 6c and 6d) (Escartín et al., 2007). Apparent fault heave, estimated from fault throw and uncorrected fault dip, ranges from ~0 to 10 m. After applying the empirical dip correction (Equation 1), fault heave is reduced to ~0–5 m (Figures 6c and 6d). Overall, uncorrected fault dips have a modal average of ~70°, which is considerably less steep than the corrected fault dip, which has a modal average >80°.

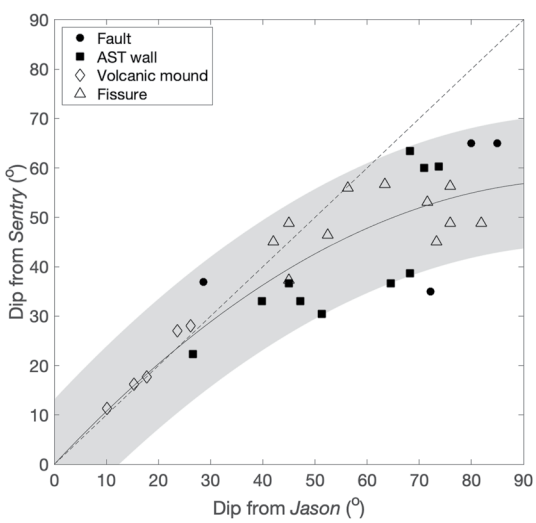


**Figure 5.** Comparison of apparent dips estimated from co-registered AUV *Sentry* and ROV *Jason* bathymetric profiles over fault scarps (filled circles), AST walls (filled square), volcanic mounds (diamonds), and fissures (triangles). Black line with gray band is second-degree polynomial fit and 95% confidence interval; dashed line is the slope of 1.

Fissures located proximal to the AST tend to be longer, while off-axis fissures tend to be shorter and clustered together in groups or swarms (Figures 1b and 1c). Across the entire survey area, the median fissure width and depth are 4.7 and 2.3 m, respectively. Fissures within the 2005–2006 eruption area are more elongated parallel to the ridge axis, whereas fissures outside the eruption area appear to be more discontinuous (Figures 1b and 1c), likely due to variability in repaving by younger lava flows. Fissures arranged in an *en échelon* pattern are found in the northern segment (Figure 1b) and off-axis area (Figure 1c), and the center of individual fissures are wider and steeper than at either end (Figures 2a–2c).

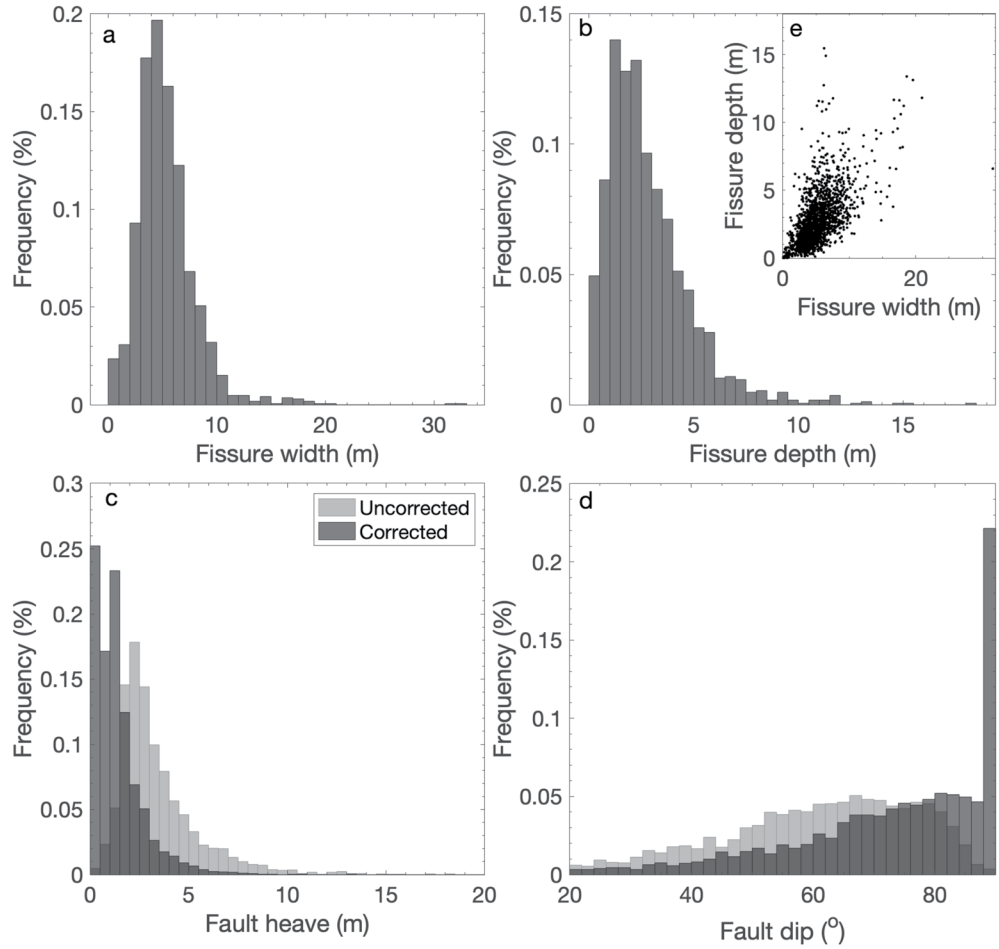


**Figure 6.** (a and b) Histograms showing the distribution of fissure width and depth, respectively, estimated from 1-m resolution *Sentry* bathymetric profiles spaced at 10 m interval crossing 381 near-axis fissures (of 707 total fissures mapped). (e) Fissure width versus fissure depth, estimated for 381 near-axis fissures. (c, d) Histograms showing distribution of fault heave and dip angle, respectively. Heave and dip angles estimated from 1-m resolution bathymetric profiles spaced at 10 m intervals crossing 38 inward fault scarps identified using multibeam bathymetric data collected by AUV *Sentry* in 2019–2021. Gray bars show uncorrected fault dip and heave from AUV *Sentry* bathymetric data; dark gray bars show fault dip and heave corrected using calibration function obtained from coincident ROV *Jason* profiles, shown in Figure 5.

To investigate spatial patterns in fissure geometry, we separated the 707 identified fissures into three groups according to their location with respect to the AST and the 2005–2006 eruption area (Figure 9). Group (1) fissures are located both within the AST and within the 2005–2006 eruption area (here called "active fissures"); group (2) fissures are located either within the AST or within the 2005–2006 eruption area but not both (here called "older fissures"); group (3) fissures are outside the AST and outside the 2005–2006 eruption area (here called "off-axis fissures"). Active and older fissures account for about half of all fissures identified (51%), while the remainder are off-axis. Active fissures are the widest, deepest, and longest fissures among the three groups (Table 1). Active and off-axis fissures are on average longer than older fissures, and active fissures are on average wider and deeper than off-axis and older fissures, and the latter two groups have comparable width and depth (Table 1). However, none of these groups exhibit systematic patterns in geometry along-axis, that is, with latitude (Figure 9).

### 4.2. Fissure Reactivation

By comparing sidescan sonar images collected before and after the 2005–2006 eruption, we can identify new or reactivated fissures and changes in fissure geometry associated with the eruptions in 2005–2006. We used towed DSL-120a sidescan sonar data acquired in 2001 (Fornari et al., 2004) to identify fissures that were present before

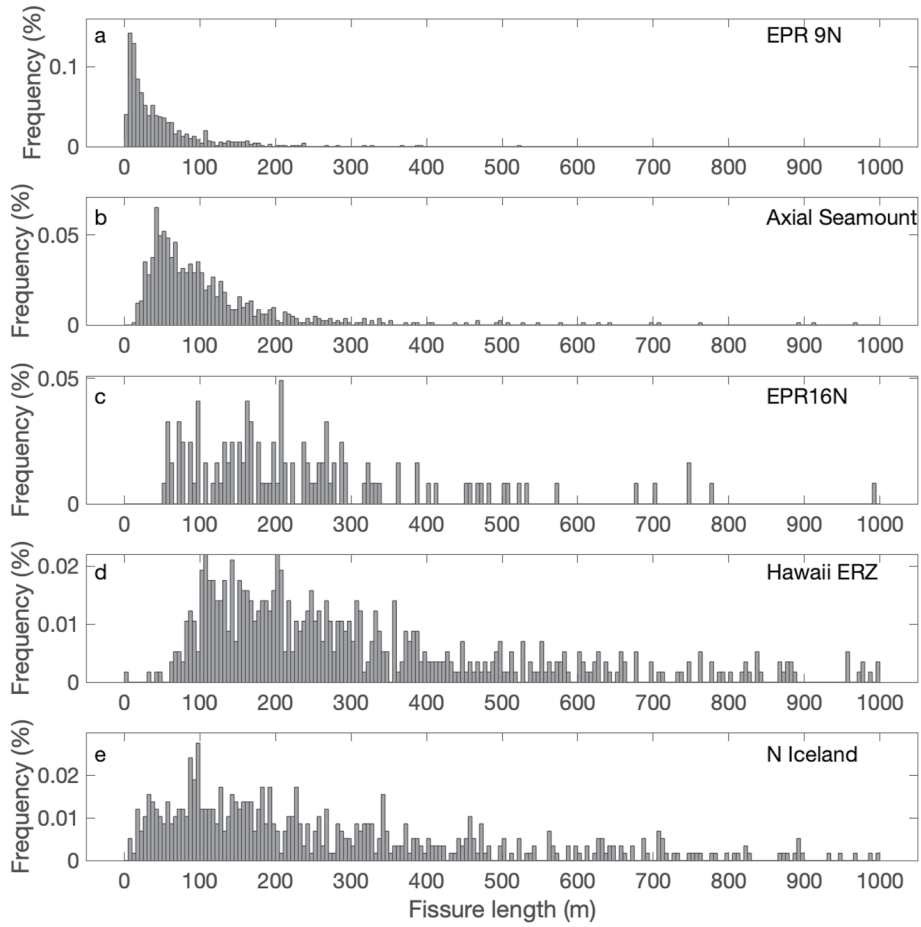


**Figure 7.** (a–e) Fissure length distribution at EPR 9–10°N (707 fissures), Axial Seamount (828 fissures), EPR 16°N (122 fissures) in comparison to Hawai'i (571 fissures) and Iceland (581 fissures) (Chadwick et al., 2014; Clague et al., 2018, 2021; Hjartardóttir, Einarsson, & Björgvinsdóttir, 2016; Hjartardóttir, Einarsson, Magnúsdóttir, et al., 2016; Le Saout et al., 2018, 2021; Sherrod et al., 2007).

the 2005–2006 eruption. These data provide good spatial coverage along the segment; however, their ability to resolve seafloor features is hampered by considerable nadir artifacts which obscure the seafloor morphology along much of the trace of the AST. Cognizant of this limitation, we compared these pre-existing sidescan sonar images with sidescan sonar images collected by AUV *Sentry* in 2019–2021 to identify three classes of fissure: (a) those not present in the 2001 data, and therefore likely formed during the 2005–2006 eruption; (b) pre-existing fissures that were paved over with new lava during the 2005–2006 eruption; (c) pre-existing fissures that were reactivated in 2005–2006 eruption (Figure 10). Despite the multiple square-kilometer spatial extent of the 2005–2006 eruptions, we estimate that fewer than five new fissures were created during those eruptive phases (Figures 10a–10c). In contrast, more than 100 fissures were either infilled with new lava or reactivated during the eruption (Figures 10d–10i). Infilled fissures appear to be either entirely paved over with new lava flows (Figures 10g–10i) or became shorter after the eruption, possibly due to partial infilling (Figures 10d–10f). Figures 10e and 10f show examples of reactivated fissures that likely sourced a lava channel that flowed from the eastern margin of the AST to the east.

### 4.3. Off-Axis Fissures and Lava Flows

Fissures within the AST tend to be isolated (Figure 11a) and oriented parallel with the local AST trend. Lava sourced from these fissures can flow over distances of up to ~4 km away from the AST, and often have smooth upper surfaces (Figure 11b). Abundant fissures are identified at the summits of several on- and off-axis (>~1 km from axis) volcanic mounds, and they tend to occur in swarms aligned in an *en échelon* pattern (Figures 1c, 11c,

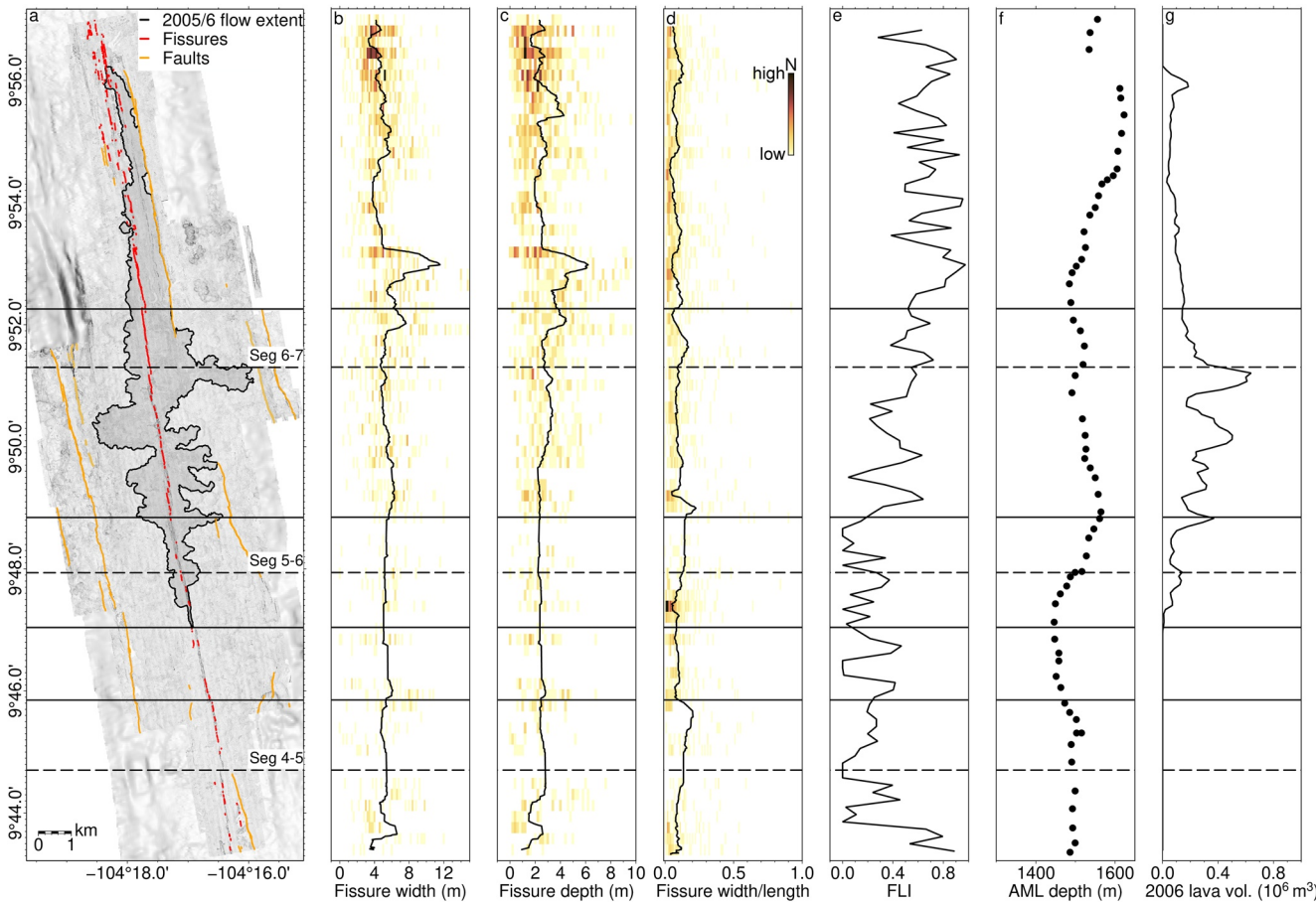


**Figure 8.** Comparison of fissure dimensions with subsurface magma system properties. (a) Faults and near-axis fissures mapped by AUV *Sentry* are red and orange lines, respectively; 2005–2006 flow extent is marked as black outline; horizontal black/red lines are tectonic/AML discontinuities, respectively (Carbotte et al., 2013; Haymon et al., 1991; Wu et al., 2022); AML discontinuities labeled following convention of Carbotte et al. (2013). (b–d) Fissure width, depth, width/length ratio versus latitude. Shading shows normalized point count density and black lines are moving average with latitude. Fissure coverage distribution (FLI = fissure length index, defined in Section 5.4). (f) AML depth (Marjanović et al., 2018); (g) 2005–2006 eruption volume, summed in 100 m-wide along-axis bins (Wu et al., 2022).

11d). Lava flows sourced from the near-axis eruptive fissures are proximal to volcanic mounds (Figures 11c and 11d), and seem to have traveled to only a few tens of meters and typically have a rougher surface morphology than those erupted on the AST (Figures 11a and 11b). Off-axis fissures near volcanic mounds might also be the source of lava flows given their spatial proximity and lava morphology nearby (Figure 12). However, based on the available data, we cannot exclude the possibility that these fissures are non-eruptive cracks, created by far-field tectonic forces.

Fissures on plateau-like lava flows with rounded levee margins can be identified at distances >2 km from the AST (Figure 12). South of the plateau-like lava flow, bathymetric low hosts a lava flow unit with a smooth, concave-down upper surface enclosed by crenulated and elevated lava levees (Figure 13). Partial mapping in this area implied that this unit extends further south with normal faults bounding its western margin near 9°46′N (Figure 14). Given the frequent re-paving of the seafloor due to the eruptive cycle length of ~8–18 years (Wu et al., 2022), abandoned fissures and older flows would be expected to be re-paved and filled by lava from more recent eruptions that originate from the axis. Although these fissures could potentially be created by tectonic forces (i.e., non-eruptive processes), we cannot rule out that they are eruptive given their coincidence with lower-crustal off-axis magma lenses (OAML). These magma bodies were identified in seismic reflection images at ~9°48′N and centered ~1.5 km from the ridge axis at 1.8 s two-way travel time below the seafloor (Aghaei et al., 2014). Fissures and low-relief flows identified off-axis here may represent an eruptive activity outside the AST, providing insight into the possible distribution of off-axis melt sources. These fissures and low relief lava flows also coincide with discontinuities in both the AST (i.e., tectonic discontinuities) and in the AML between

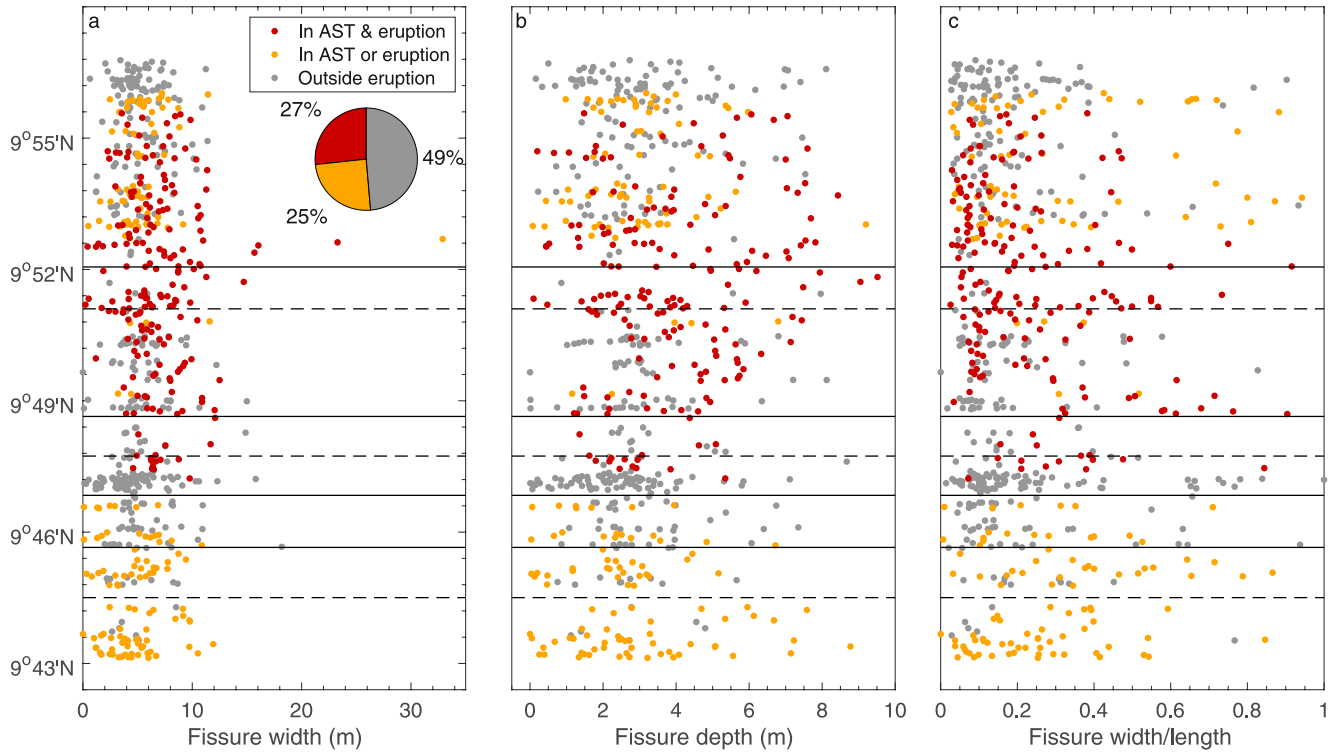


**Figure 9.** Fissures ($n = 707$) categorized by setting versus latitude. (a) Colored dots are fissures divided into three groups: inside the AST *and* inside the 2005–2006 eruption area (red; Figure 1; Wu et al., 2022); inside the AST *or* inside the 2005–2006 eruption area (yellow); outside both the AST *and* the eruption area (gray); pie chart gives overall relative proportions of each setting. (b and c) Fissure width and fissure width/length versus latitude, colored according to groups described in (a).

segments 6 and 7 (as defined by Carbotte et al. (2013)). These structures could represent an off-axis magma source and plumbing system that is distinct from the main AML that sources melts and lava eruptions within and proximal to the AST.

## 5. Discussion

### 5.1. Graben and Non-Axis Parallel Faults

Most faults formed in the 9°50′N segment of the EPR strike parallel to the ridge axis and often create substantial grabens (e.g., Escartín et al., 2007), which can be found on both flanks of the ridge (Figures 15 and 16). The tens of meters of relief on these grabens can inhibit the advance of lava flows off-axis (e.g., Soule et al., 2007; Figures 15 and 16). Locally, stair-case structures on inward facing faults imply multiple faulting episodes rather than a single slip event on a single surface (Figures 15d, 15e, 15f, and 16c). Lava flows are commonly observed partly burying the outward facing slope and floors of the graben; this lava infilling may result in an underestimation of fault dip (Figures 15 and 16).

**Table 1**
*Summary of Observed Fissure Geometries, Grouped According to Position Relative to the AST and the 2005–2006 Eruption Area*

| | Median width (m) | Median depth (m) | Median length (m) |
|---|---|---|---|
| Active | 6.4 ± 3.0 | 3.8 ± 2.5 | 34.6 ± 4.2 |
| Older | 4.9 ± 3.2 | 2.5 ± 2.3 | 16.9 ± 2.1 |
| Off-axis | 4.7 ± 2.5 | 2.7 ± 2.4 | 34.6 ± 4.3 |

*Note*. "Active" fissures (186 fissures) are those located within the AST and within the 2005–2006 eruption area; "older" fissures (172 fissures) are located within the AST or the 2005–2006 eruption area (but not both); "off-axis" fissures (339 fissures) are located outside the AST and outside the 2005–2006 eruption area.

There are two notable faults located around AML discontinuities (as defined in Carbotte et al. (2013)) and fourth-fourth order tectonic discontinuities (as defined in Macdonald et al. (1992)) at 9°44.6′N and 9°48′N, that are not parallel to the ridge axis (Figure 17). Both discontinuities have orientations resulting in an increasing distance from the ridge crest in the southward direction, and both have the fault throws that increase in the southward direction (Figure 17b). The fault at ~9°48′N is oriented in a more oblique direction to the axis (Figure 17a) and its location is coincident with an OAML imaged by seismic reflection data (Aghaei et al., 2017).

10.1029/2022GC010794

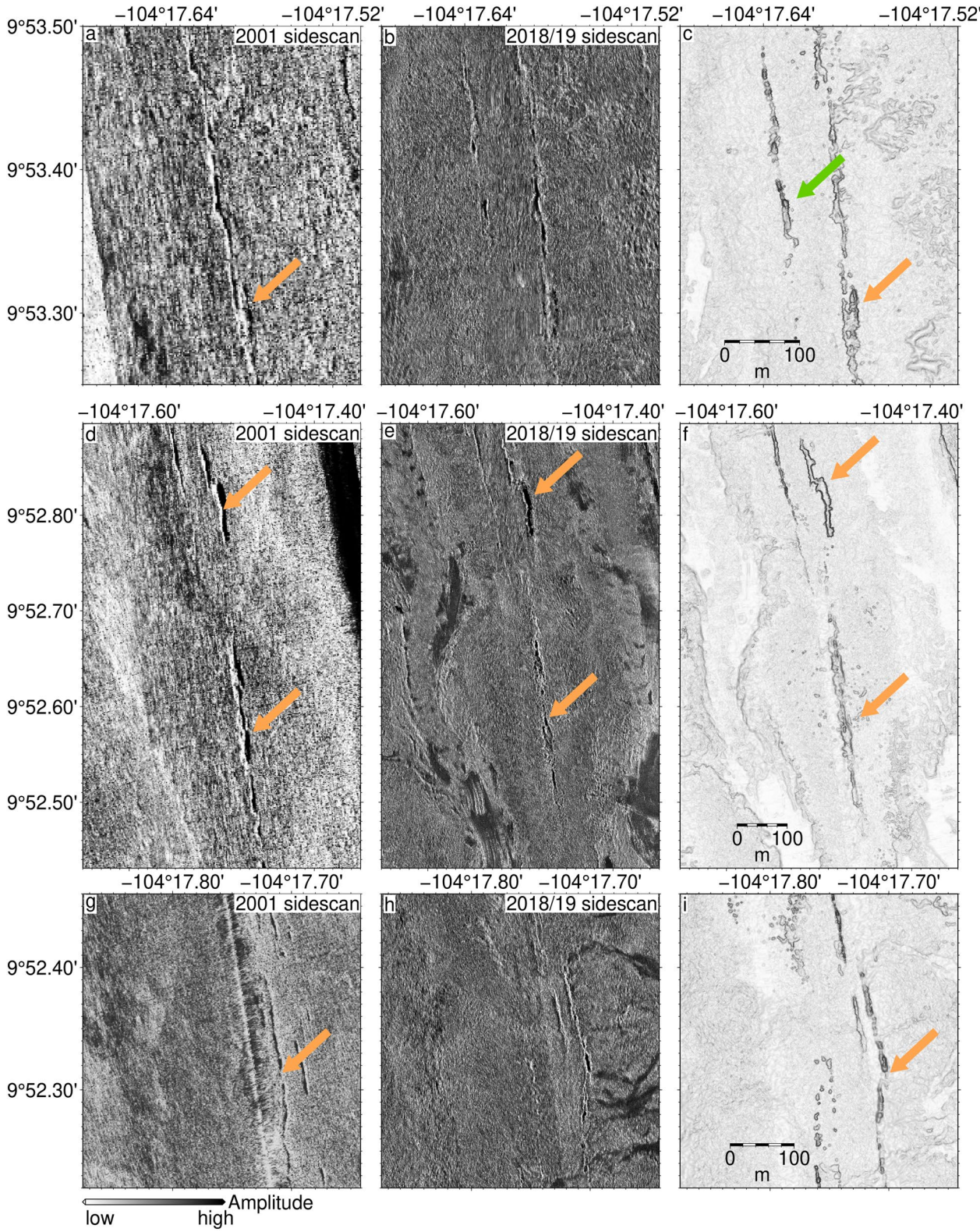


**Figure 10.** Examples of fissures mapped before and after the 2005–2006 eruptions. (a and b) and (d and e) and (g and h): Sidescan images acquired with towed DSL-120A sonar (cruise AT07-04, 2001; Fornari et al., 2004) and with EdgeTech 2200M sonar using AUV *Sentry* (cruise AT42-21, 2019; Wu et al., 2022), respectively. (c, f, and i) Shaded gray-scale bathymetry. Green arrow shows a tentatively identified fissure created between 2001 and 2019, likely during the 2005–2006 eruption; orange arrows show fissures likely reactivated during the 2005–2006 eruption.

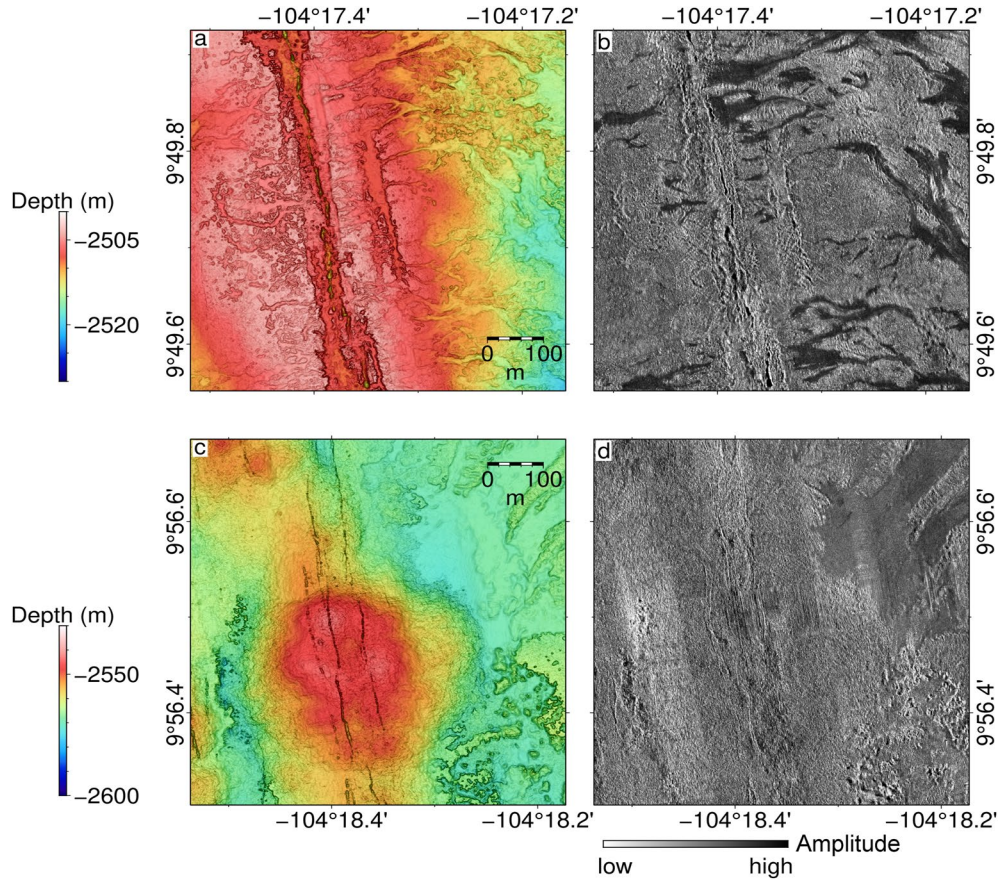


**Figure 11.** Examples of fissures on volcanic mounds and within and proximal to the AST. (a and b) Bathymetry and sidescan image of fissures in the AST that sourced the 2005–2006 eruption, respectively. (c and d) Bathymetry and sidescan images of fissures on top of volcanic mounds, respectively.

### 5.2. Tectonic Strain Estimate

The cumulative horizontal displacement, $D$, due to fault slip is calculated along each profile using

$$D = t \tan^{-1} \theta, \tag{2}$$

where $t$ is fault throw (measured along-profile), and $\theta$ is fault dip. The presence of mass-wasted material at the base of footwall scarps (i.e., talus) has the effect of reducing average apparent fault dip. Following previous approaches to overcome this problem, we use the maximum fault scarp dip for the purposes of estimating heave (e.g., Escartín et al., 1999; Le Saout et al., 2021). The tectonic strain, $T$, accommodated by faulting is given by

$$T = \left(\frac{D}{L}\right)100, \tag{3}$$

where $L$ is profile length. The total tectonic strain is then determined by adding cumulative along-profile fissure width to $D$, and with an average spreading rate of 110 mm/yr (Carbotte & Macdonald, 1992) the calculated estimates reflect the average strain over the last ~40 kyr. The total tectonic strain averaged between 9°43′–57′N with uncorrected fault dip is ~0.22% ± 0.26%, and with the corrected fault dip is ~0.15% ± 0.23%. We note that the outward facing faults accommodate negligible amounts of strain (~0.008%), or ~5% of the total tectonic strain. These estimates are much smaller than previous strain estimates (0.7%) made using deep-tow camera and submersible profiles with the assumption of a constant 45° fault dip (Escartín et al., 2007). For the EPR crest in the study area, values for the combined extension accommodated by faults and fissures are ~0.21 and ~0.13 mm/yr for uncorrected and corrected fault dips, respectively. These estimates represent lower bounds due

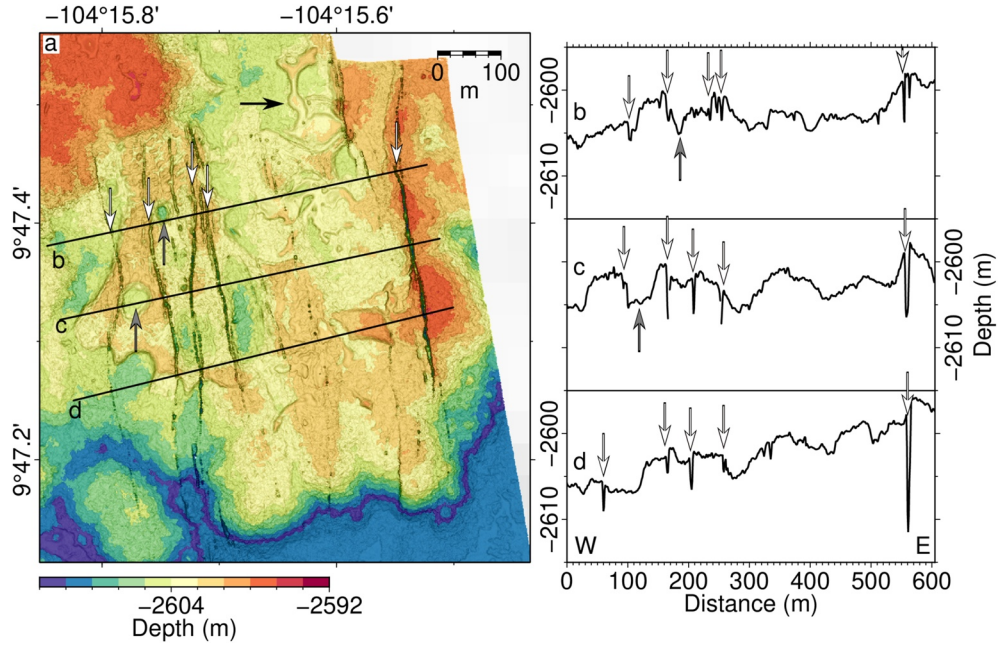


**Figure 12.** Fissure swarm near 9°47.3′N, ~2.3 km east of the AST, associated with a low relief flow and coincident with an OAML (see Figure 1 for location). (a) Bathymetry showing smooth, lobate and domed constructs of the inflation plateau, cross-cut by sub-parallel, ~north-south trending fissures. Black lines represent bathymetric profiles (b–d); white arrows point to individual fissures, also shown in panels (b–d); black arrow shows lobate (pressure) ridge; gray arrows show pressure rise pits. (b–d) Bathymetric profiles oriented from west to east showing fissure and plateau geometry; note that easternmost fissure is up to 12 m deep, and 2 m wide.

to the potential for post-extension lava flows, which could partially or fully obscure fault scarps (e.g., Carbotte et al., 1997). The tectonic strain estimates represent the component of brittle deformation in a narrow (<4 km) axial zone above the AML, while larger estimates might be obtained further off-axis (>4 km), which was previously suggested to be associated with plate bending (Escartín et al., 2007).

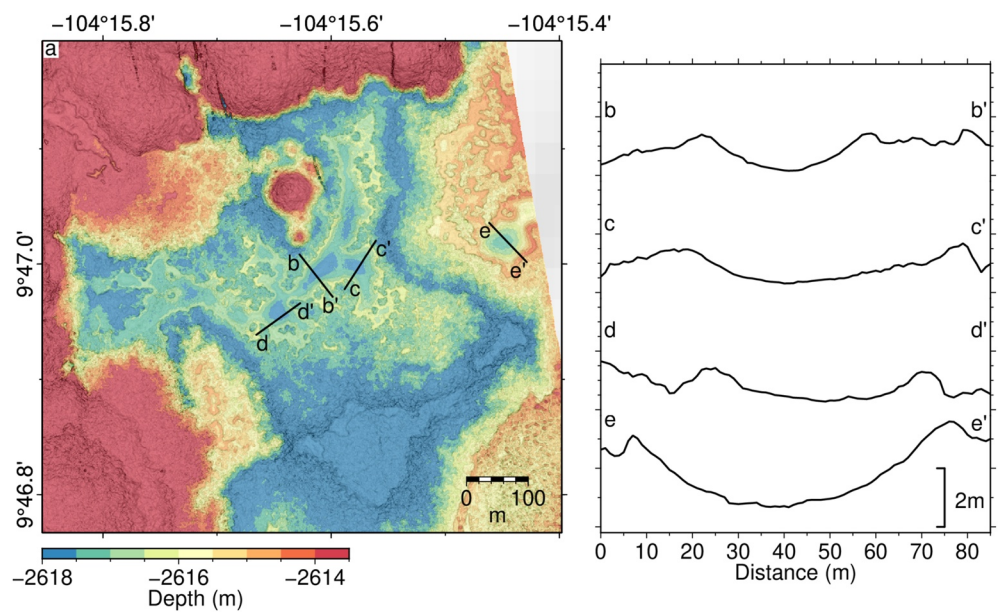


**Figure 13.** (a) Off-axis low relief flow, located ~2.3 km east of the AST (see Figure 1 for location); black lines show locations of profiles (b–e). (b–e) Bathymetric profiles across sag basins, note smooth character of lava flow bounded between rounded levees.

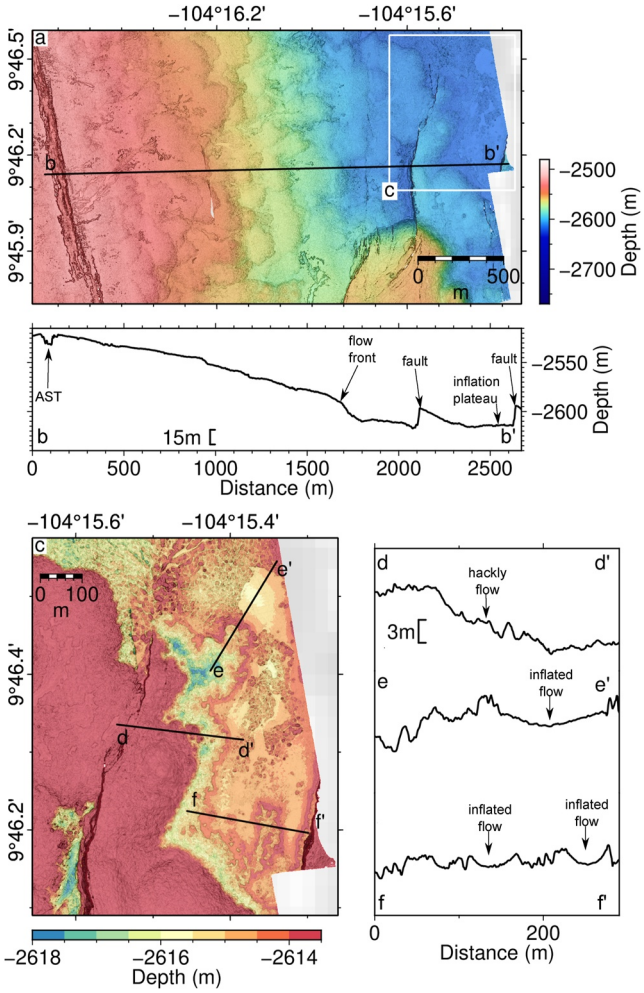


**Figure 14.** An example of off-axis lava plateau near 9°46.4′N, ~2.4 km east of the AST. (a) and (b) Map and cross-section showing AST, flow front, lava plateau, and fault scarps; white box shows the location of (c). (c) Detailed map of off-axis inflated flow; black lines show locations of profiles (d–f). (d) Profile showing hackly lava flow from axis covering over the fault scarp. (e) and (f) Examples of sag basins associated with lava plateau.

### 5.3. Spatial Variations in Fissure Geometry

As primary conduits of magma outflow at the seafloor, the length scale of eruptive fissures is thought to correlate with the geometry of dikes that transport magma from the AML in primary fissures, which in turn play an important role in plate separation (e.g., Valentine & Perry, 2006). Positive relationships between eruptive fissure length and spreading rate have been proposed to support the idea that fast-spreading ridges yield longer fissures than slower-spreading ridges due to enhanced lateral magma transport (Sinton et al., 2002). To test this idea, we compare fissure geometry estimated from four other study sites where detailed meter-scale mapping is available (EPR 16°N; Axial Seamount; Iceland Northern Volcanic Zone; NVZ, and Kilauea's East Rift Zone; ERZ in Hawai'i; Table 2). This preliminary comparison does not support the idea that fissure length is positively correlated with the spreading rate. Although fissure length estimates can be hampered by the limitations of submarine field observations, we find that fissure lengths at the two land-based study sites (Hawai'i and Iceland) are an order of magnitude longer than the fissures mapped at 9°50′N EPR and at Axial Seamount. Welch's *t*-tests between every combination of fissure length distribution pairs reject the null hypothesis, indicating that the two populations are significantly different at 5% significance level ($p < 0.05$), except for the pair of Hawai'i ERZ and Iceland NRZ, which fails to reject the null hypothesis ($p = 0.6$; Figure 7). Although fissure length is highly variable at each MOR segment (as evidenced by high standard deviation estimates), these comparisons show that median fissure length is probably unrelated to the spreading rate.

Fissure formation is likely to be related to the geometry and dynamics of the underlying magmatic feeder system, including processes such as diking and inflation/deflation of a magma lens (e.g., Hjartardóttir et al., 2009; Tentler & Temperley, 2007). To examine the relationships between fissure geometry and the magmatic system at the EPR 9°50′N segment, we compared spatial patterns in fissure geometry to the properties of the underlying magmatic system based on estimates of AML depth (Marjanović et al., 2019), and the surface extent of the 2005–2006 eruptions (Wu et al., 2022; Figure 8). In this analysis, we used only the fissures located near-axis (<1 km), that is, those that are assumed to be eruptive. There is little evidence for spatial correlation between fissure geometry (i.e., width, depth, and aspect ratio) and AML depth, nor with the spatial distribution of surface lava associated with the 2005–2006 eruption (Wu et al., 2022). Fissure geometry seems to be uniform as a function of latitude along-axis, regardless of whether they are located directly above a melt source imaged using multichannel seismic techniques. Although our fissure geometry estimates are likely biased by repeated lava burial and infilling, this consistent spatial distribution implies that subsurface magma lens geometry and the locus of the 2005–2006 eruptions have only limited impacts on the distribution of fissures. It is more likely that the geometry of fissures is dominated by far-field extensional forces on longer timescales, with shorter timescale eruption cycles playing a secondary role. This interpretation is consistent with the idea that individual fissure geometry is dominated by factors other than the localized distribution of subsurface melt (e.g., Lundgren et al., 2013; Neal et al., 2019).

Changes in fissure geometry before and after the 2005–2006 eruptions provide evidence that fissures are often reactivated during successive eruptions. For example, during the 2011 eruption at the Axial Seamount, lava erupted primarily from reactivated fissures along the south rift zone that had previously fed the 1998 eruption (Caress et al., 2012; Chadwick et al., 2013; Clague et al., 2017). In 1998, the median eruptive fissure length in the Axial Seamount segment was ~608 m, decreasing to ~178 m after the 2011 eruption (Chadwick et al., 2014; Clague et al., 2017, 2018a). The 2015 eruption area contains ~24 lava flows located mostly north of the caldera. Fissures that were active during the 1998 and 2011 eruptions were not reactivated in 2015. The median fissure length for the 2015 eruption was ~496 m (Clague et al., 2018b).

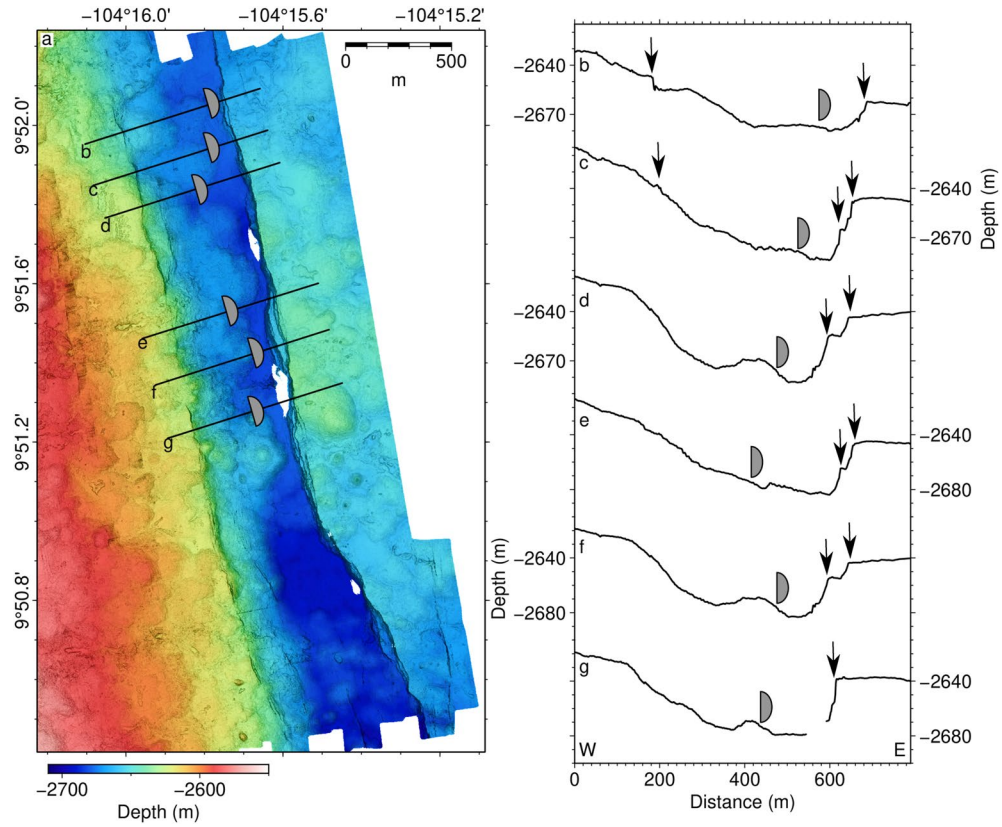


**Figure 15.** Example of graben east of the EPR axis partly in-filled with lava flows sourced from the axis to the west (location shown in Figure 1). (a) Bathymetry of graben. (b–g) Bathymetric profiles across graben; black arrows mark faults; gray infilled arcs mark lava flow lobe front.

An example of subaerial fissure reactivation in Iceland comes from satellite imagery showing that an eruptive fissure created in 1897 was reactivated and shortened in length during the 2014 eruption in central Iceland (Ruch et al., 2016). Smaller-scale shortening of fissures was also observed following the 2005–2006 eruptions at the 9°50′N area of the EPR (Figures 10d–10f). Because dikes that penetrate the volcanic layer at MORs are mostly vertical or near-vertical (Karson, 2002; Karson et al., 2002), the reactivation of a fissure is likely to be associated with an array of parallel, side-by-side dikes over time (i.e., sheeted dike complexes) beneath the spreading axis (Karson et al., 2015). Terrestrial field observations and analog and numerical models show that the total horizontal extension associated with a vertical magmatic intrusion is likely to be about two-thirds the width of the dike itself (Mastin & Pollard, 1988). Based on ophiolite field observations, dikes are expected to have an average width of 1 m (e.g., Gudmundsson, 1995; Harper, 1984). Assuming that all horizontal extension due to subsurface dikes is recorded by the opening of fissures, the observed median fissure width of 4.7 m for the EPR 9°50′N study area would require roughly seven 1 m-wide dikes to form. Since some of the plate separation could be accommodated further off-axis (>4 km) by tectonic extension (e.g., Escartín et al., 2007), our estimate indicates that the plate separation in the axial zone is mostly accommodated by magmatic diking (99.5%–100%). Considering only the near-axis area, a magmatic event recurrence interval can be estimated from the dike width and spreading rate. If the average combined dike width beneath each fissure is ∼7 m (i.e., 3/2 the fissure width), which should accommodate the full plate separation rate of 110 mm/yr (Carbotte & Macdonald, 1992), then the time needed to inject the necessary dikes beneath each fissure is about 64 years. This finding implies a periodicity of magmatic diking events of ∼9 yr (that it, seven 1 m-wide dikes in 64 years), which is consistent with independent estimates of recurrance interval from lava flow volume and melt extraction calculations (Wu et al., 2022; Xu et al., 2014).

A notable area interpreted to host off-axis volcanism is located ∼2.3 km east of the axis near 9°47.3′ (Figure 12), where fissures up to ∼550 m long and ∼12 m deep are identified. These fissures are associated with smooth, lobate, domed constructs (Figures 12 and 13). These plateau-like flows are consistent with submarine inflated lava flows identified elsewhere that are sustained by long-lasting, moderate effusion rates (e.g., Deschamps

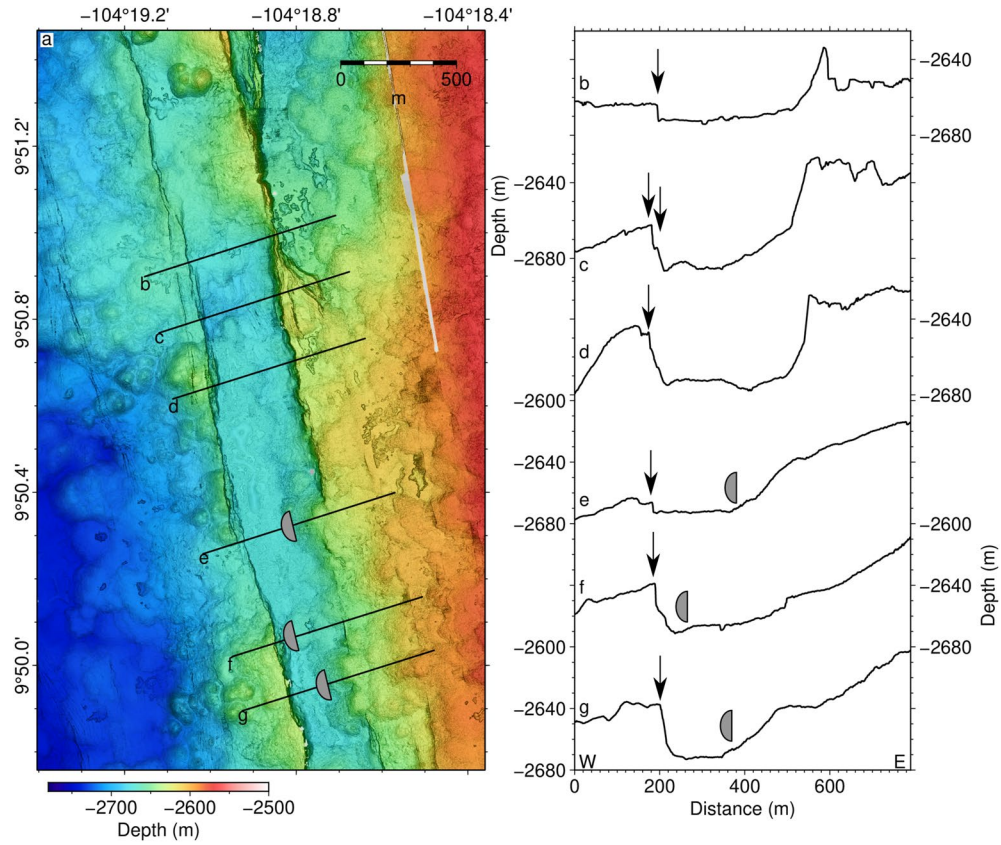


**Figure 16.** Example of a graben west of the EPR axis, partly in-filled with lava flows sourced from the east (location shown in Figure 1). (a) Bathymetry of graben. (b–g) Bathymetric profiles across graben; black arrows mark faults; gray infilled arcs mark lava flow lobe front.

et al., 2014), resulting in remarkably smooth surfaces with well-defined sag basins in areas with slopes <2° (Self et al., 1996). Previously documented subaqueous examples include inflated flows on the Axial Seamount on the Juan de Fuca Ridge, at 16°N on the crest of the EPR, and at the summit of the Galápagos spreading center (Appelgate & Embley, 1992; Chadwick et al., 2013; Clague et al., 2013; Deschamps et al., 2014; McClinton et al., 2013).

South of the fissures near 9°47′N (Figure 12), a bathymetric depression hosts a plateau with ~3 m of relief, crenulated margins, and a concave surface shape that indicates likely post-eruption deflation or drain-out (Figure 13). This plateau is interpreted to have been locally fed and ponded in an area of low pre-existing relief (Figure 13). There is an additional plateau to the south and east, which is only partially covered by near-bottom mapping data; however, its geometry suggests an eruptive source further to the east, although further data are required to confirm this relationship (Figure 14). The southern portion of this partially mapped flow is characterized by 2–3 m of relief, and a complex system of sag basins, crenulated lobes, lava breakouts, and regions of hackly and hummocky texture. The fault scarps apparently bounding the flow to the south have 15–18 m of vertical relief (Figure 14b) and appear to have blocked the low-lying area from flows encroaching from the axis (i.e., eruptions originating from the west).

These off-axis flows and fissure swarms coincide with the location of one of two proximal OAML identified in seismic reflection images at ~9°48′N and centered ~1.5 km from the ridge axis at 1.8 s two-way travel time below the seafloor (Aghaei et al., 2014). This location also coincides with discontinuities in both the AST (i.e., tectonic) and in the AML between segments 6 and 7 (as defined by Carbotte et al. (2013)) and could represent an off-axis magma source and plumbing system that is distinct from the main AML supplying the AST.

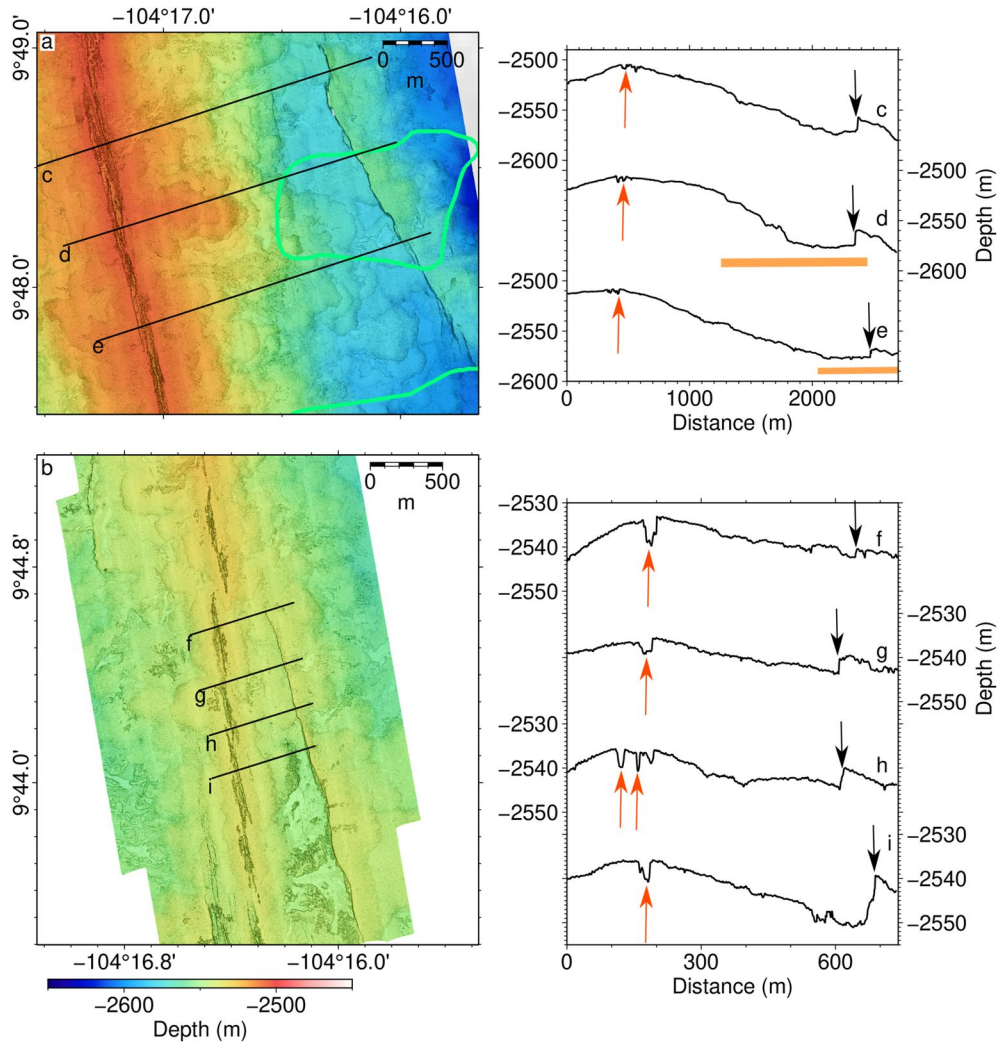


**Figure 17.** Example of graben east of the EPR axis (locations shown in Figure 1). (a and b) Bathymetry of faults oriented obliquely to the EPR axial trend. Light green polygons are OAML locations from Aghaei et al. (2017). (c–e and f–i) Bathymetric profiles across oblique faults; black arrows mark faults; orange arrows mark AST; orange bars represent OAML locations along the profiles.

**Table 2**
*Comparison of Fissure Length and Spreading Rate From the EPR, Hawai'i and Iceland*

| Region | Median fissure length (m) | Spreading rate (mm/yr) | Number of fissures |
|---|---|---|---|
| EPR 9°50′N (this study) | 29 ± 2 | ~110[a] | 707 |
| EPR 16°N[b] | 203 ± 16 | ~85[c] | 122 |
| Axial Seamount, south rift zone[d] | 80 ± 3 | ~50[e] | 889 |
| Iceland, northern volcanic zone[f] (Krafla, Barðarbunga, Askja) | 217 ± 14 | ~20[g] | 581 |
| Hawai'i: Kilauea East Rift zone[h] | 255 ± 10 | N/A | 571 |

[a]Carbotte and Macdonald (1992). [b]Le Saout et al. (2018). [c]Weiland and Macdonald (1996). [d]Chadwick et al. (2014), Clague et al. (2018a, 2021), and Le Saout et al. (2021). [e]DeMets et al. (2010). [f]Hjartardóttir, Einarsson, and Björgvinsdóttir (2016) and Hjartardóttir, Einarsson, Magnúsdóttir, et al. (2016). [g]DeMets et al. (1994). [h]Sherrod et al. (2007).

### 5.4. Fissure Distribution and Crack Depth

Although on-axis fissure geometry seems to have little relation to AML geometry and the spatial distribution of 2005–2006 eruption lava (Figure 8), fissure formation is likely to be driven by magmatic diking given that the plate separation is mostly accommodated by diking over short timescales near the axis (Escartín et al., 2007). To further investigate the mechanism of fissure initiation with respect to the AST, we quantify a simple moving average of the ratio between fissure length that covers an along-axis window and the along-axis window length (~200 m), which we term the fissure length index (FLI). The window length was chosen to cover ~90% of fissures based on the fissure length distribution (Figure 7). Where fissure coverage extends the full length of the along-axis window length, FLI = 1, whereas if no fissures are present, FLI = 0. FLI is relatively low in the area south of 9°48.5′N, which is consistent with the fact that little to no new lava was emplaced there during the 2005–2006 eruption (Figures 8e and 8g). In the central portion of the main 2005-2006 eruptions, FLI is relatively high since these fissures are likely to have fed new lava channels. Relatively high FLI north of 9°52′N is coincident with two linear fissure systems which delivered lava to the seabed during 2005–2006 eruption (Figure 8e). The high FLI at this latitude does not correlate with maximal lava volumes because the fault scarp likely diverted flows to the north and south (Figures 8e and 8g). Assuming that subsurface dikes and pathways are connected when multiple individual fissures are within several meters of each other (each fissure could still be short), values of FLI closer to 1 represent elongate single eruptive fissures. Therefore, the observed positive relationship between FLI and eruption volume (Figure 8) is consistent with the positive correlation between the eruptive fissure length and lava flow length proposed by numerical modeling (Mériaux et al., 2022).

Based upon simplified relations derived from fracture mechanics, tensile crack width (i.e., fissure width) can be used to estimate tensile crack depth (Nur, 1982). Dikes and faults can be described as internally pressurized planar cracks that propagate due to dilation by fluid injection (e.g., Rubin, 1992; Rubin & Pollard, 1988). Cracks in this model initiate at depth and propagate both up and down as they lengthen. Crack depth, $z_0$, can be defined as

$$z_0 = \frac{\left(\frac{G}{1-\nu}\right)\left(\frac{w}{2}\right)}{\sigma}, \tag{4}$$

where $G$ is the static shear modulus, $\nu$ is Poisson's ratio, $w$ is the tensile crack width, and $\sigma$ is tensile stress (Lister & Kerr, 1991; Rubin, 1990, 1992). For the purposes of comparison, the parameters used here to estimate crack depth from fissure width are taken from previous crack analysis in the 9°50′N segment, which were based on both visual observations and analysis of analog near-bottom sidescan data collected using the ARGO towed vehicle in 1989 (Haymon et al., 1991; D. J. Wright, Haymon, & MacDonald, 1995 and references therein). Fissures in this part of the analysis are within 1 km of the axis and therefore are assumed to be eruptive. For each individual fissure, average and maximum fissure widths were used to estimate the upper and lower bounds of crack depth, respectively. Crack depth derived from fissure width (Figure 8) is much deeper than the fissure depth measured at the surface (Figure 6). Such differences can be explained as the result of repeated cycles of lava emplacement during multiple eruptions, and lava drainback that partially fills eruptive fissures during the waning stages of an eruption (e.g., Wadsworth et al., 2015). The occurrence and distribution of microearthquakes detected in the build-up to the 2005–2006 eruptions, which are inferred to be caused by hydrothermal circulation and possibly melt migration (Tolstoy et al., 2008; Waldhauser & Tolstoy, 2012), do not correlate with variations in crack depth. This lack of correlation implies that fissure initiation may not be associated with brittle deformation immediately before an eruption, although a more detailed interpretation is limited by the time scale of the microearthquake observations. We find that the inferred crack depth is up to ~500 m near 9°53′N and hence exceeds the typical depth to the top of Layer 2A (which is expected to be 120–150 m below seafloor; Marjanovic et al., 2018; Figure 18). The 9°53′N area is also where FLI is high and AML depth is relatively shallow (~1,490 mbsf) (Figure 8). The AML is also relatively shallow near 9°47′N, but cracks are shallower than those near 9°53′N. This difference might be caused by the uncertainty in AML depth or that fissure widths around 9°47′N are underestimated due to infilling of lava pillar mounds (e.g., Wu et al., 2022). These relationships are consistent with the idea that the fissure formation in association with diking is favored where the AML is shallow, and that cracks feeding surface fissures extend into the sheeted dikes present in oceanic layer 2A (e.g., Karson, 2002).

## 6. Conclusions

Near-bottom, meter-resolution multibeam bathymetric data were used to identify and analyze 38 inward-facing fault scarps, four outward-facing scarps and 707 seafloor fissures on the EPR crest between 9°45′ and 9°57′N.

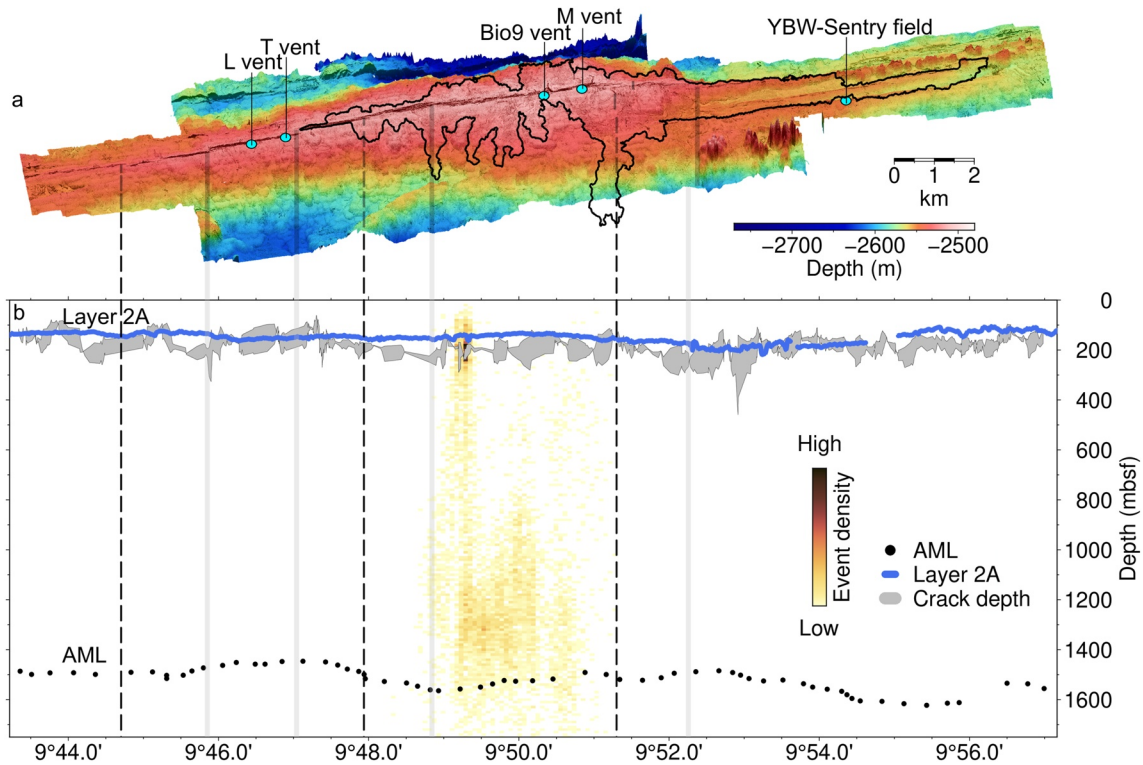


**Figure 18.** (a) 3d perspective view of 1-m resolution bathymetry; labeled blue circles are selected high-temperature hydrothermal vents; black outline is 2005–2006 eruption extent (Wu et al., 2022). (b) Black dots and blue line are AML and Layer 2A depth, respectively; colored dots are microearthquake density of events that occurred between October 2003 and April 2004 (Waldhauser & Tolstoy, 2012); gray band represents crack depth range estimated from fissure cracking model (D. J. Wright, Haymon, & MacDonald, 1995); mbsf: meters beneath the sea floor.

Comparison of depth profiles and imagery from ROV *Jason* shows that fault dip estimated from AUV-based bathymetric data is likely underestimated by up to 30% for faults that dip >60°. After applying an empirical dip correction, we find that faults within ~2 km of the spreading axis are mostly near-vertical, indicating that horizontal tectonic strain accommodated by normal faulting in the near-axis zone must be negligible (<1%). Eruptive fissures identified in sidescan sonar images acquired both before and after the 2005–2006 eruptions show that most of the eruptive fissures were reactivated. A comparison with eruptive fissures in other spreading environments (both submarine and land-based) shows that fissure length is more likely to be affected by reactivation and infilling during successive eruption cycles than the spreading rate over short (~10–100 yr) time periods. Although we find that fissure geometry is not strongly related to the subsurface geometry of the axial magma lens, fissure formation and distribution are probably closely linked to diking events. Based on a preliminary analysis of the relationships between fissure width and underlying diking width, we estimate a diking recurrence interval of ~9 years for the EPR between ~9°45 and 9°57′N, which is consistent with other estimates of magmatic episode timing for this location. Crack depths estimated from near-axis eruptive fissure widths suggest that conduit availability to subsurface magma may control eruptive fissure geometry. We interpret the presence of fissure swarms and concave-shaped lava flows at distances >2 km from the AST to indicate sustained off-axis volcanism at low effusion rates and ponding of flows in closed depressions fed by off-axis magma lenses. These observations suggest that volcanism and subsurface heat sources may be present across a broader cross-axial zone than previously thought for the study area.

## Data Availability Statement

Multibeam bathymetric and sidescan sonar data collected by AUV *Sentry*, and fault and fissures and 2005–2006 flow margin outline shapefiles are available at the Marine Geoscience Data System at https://doi.org/10.26022/IEDA/330373, https://doi.org/10.26022/IEDA/330374, and https://doi.org/10.26022/IEDA/330841.

**Acknowledgments**
The authors thank the officers and crews of RV *Atlantis* and RV *Roger Revelle*, and the *Sentry*, *Alvin* and *Jason* operations teams and scientific parties for their professionalism during cruises AT42-06, AT42-21, and RR2102. We thank W. Chadwick, M. Le Saout, and an anonymous reviewer for their insightful comments which improved our work. We thank Ásta Rut Hjartardóttir for kindly providing a database of fissures from the Northern Rift Zone of Iceland. Figures were plotted with Generic Mapping Tools version 6 (Wessel et al., 2019). This project is supported by National Science Foundation Grants OCE-1834797, OCE-1949485, OCE-194893, OCE-1949938, and by the Scripps Institution of Oceanography's David DeLaCour Endowment.

## References

Aghaei, O., Nedimović, M. R., Carton, H. D., Carbotte, S. M., Canales, J. P., & Mutter, J. C. (2014). Crustal thickness and Moho character of the fast-spreading East Pacific Rise from 9°42′N to 9°57′N from poststack-migrated 3-D MCS data. *Geochemistry, Geophysics, Geosystems*, *15*(3), 634–657. https://doi.org/10.1002/2013GC005069.Received

Aghaei, O., Nedimović, M. R., Marjanović, M., Carbotte, S. M., Pablo Canales, J., Carton, H., & Nikić, N. (2017). Constraints on melt content of off-axis magma lenses at the East Pacific Rise from analysis of 3-D seismic amplitude variation with angle of incidence. *Journal of Geophysical Research: Solid Earth*, *122*(6), 4123–4142. https://doi.org/10.1002/2016JB013785

Appelgate, B., & Embley, R. W. (1992). Submarine tumuli and inflated tube-fed lava flows on Axial Volcano, Juan de Fuca Ridge. *Bulletin of Volcanology*, *54*(6), 447–458. https://doi.org/10.1007/BF00301391

Behn, M. D., & Ito, G. (2008). Magmatic and tectonic extension at mid-ocean ridges: 1. Controls on fault characteristics. *Geochemistry, Geophysics, Geosystems*, *9*(8), Q08O10. https://doi.org/10.1029/2008GC001965

Bohnenstiehl, D. W. R., & Carbotte, S. M. (2001). Faulting patterns near 19°30′S on the East Pacific Rise: Fault formation and growth at a super-fast spreading center. *Geochemistry, Geophysics, Geosystems*, *2*(9), 1056. https://doi.org/10.1029/2001GC000156

Buck, W. R., Lavier, L. L., & Poliakov, A. N. B. (2005). Modes of faulting at mid-ocean ridges. *Nature*, *434*(7034), 719–723. https://doi.org/10.1038/nature03358

Canales, J. P., Carton, H., Carbotte, S. M., Mutter, J. C., Nedimović, M. R., Xu, M., et al. (2012). Network of off-axis melt bodies at the East Pacific Rise. *Nature Geoscience*, *5*(4), 279–283. https://doi.org/10.1038/ngeo1377

Carbotte, S. M., & Macdonald, K. C. (1992). East Pacific Rise 8°-10°30′N: Evolution of ridge segments and discontinuities from SeaMARC II and three-dimensional magnetic studies. *Journal of Geophysical Research*, *97*(B5), 6959–6982. https://doi.org/10.1029/91jb03065

Carbotte, S. M., Mutter, J. C., & Xu, L. (1997). Contribution of volcanism and tectonism to axial and flank morphology of the southern East Pacific Rise, 17°10′-17°40′S, from a study of layer 2A geometry. *Journal of Geophysical Research*, *102*(B5), 10165–10184. https://doi.org/10.1029/96jb03910

Carbotte, S. M., Marjanović, M., Carton, H., Mutter, J. C., Canales, J. P., Nedimović, M. R., et al. (2013). Fine-scale segmentation of the crustal magma reservoir beneath the East Pacific Rise. *Nature Geoscience*, *6*(10), 866–870. https://doi.org/10.1038/ngeo1933

Caress, D. W., Clague, D. A., Paduan, J. B., Martin, J. F., Dreyer, B. M., Chadwick, W. W., et al. (2012). Repeat bathymetric surveys at 1-metre resolution of lava flows erupted at Axial Seamount in April 2011. *Nature Geoscience*, *5*(7), 483–488. https://doi.org/10.1038/ngeo1496

Chadwick, W. W., Clague, D., Perfit, M., Paduan, J., Merle, S., Embley, R., et al. (2014). Interpreted outlines as shapefiles of the 1998 lava flows and eruptive fissures at Axial Seamount, Juan de Fuca Ridge (investigator William Chadwick). *Integrated Earth Data Applications (IEDA)*. https://doi.org/10.1594/IEDA/321222

Chadwick, W. W., Clague, D. A., Embley, R. W., Perfit, M. R., Butterfield, D. A., Caress, D. W., et al. (2013). The 1998 eruption of Axial Seamount: New insights on submarine lava flow emplacement from high-resolution mapping. *Geochemistry, Geophysics, Geosystems*, *14*(10), 3939–3968. https://doi.org/10.1002/ggge.20202

Chorowicz, J., Collet, B., Bonavia, F. F., & Korme, T. (1994). Northwest to north-northwest extension direction in the Ethiopian rift deduced from the orientation of extension structures and fault- slip analysis. *Geological Society of America Bulletin*, *106*(12), 1560–1570. https://doi.org/10.1130/0016-7606(1994)105<1560:NTNNED>2.3.CO;2

Clague, D. A., Paduan, J., Caress, D., Chadwick, W., Le Saout, M., Dreyer, B., & Portner, R. (2017). High-resolution AUV mapping and targeted ROV observations of three historical lava flows at Axial Seamount. *Oceanography*, *30*(4). https://doi.org/10.5670/oceanog.2017.426

Clague, D. A., Caress, D. W., Dreyer, B. M., Lundsten, L., Paduan, J. B., Portner, R. A., et al. (2018). Geology of the Alarcon Rise, southern Gulf of California. *Geochemistry, Geophysics, Geosystems*, *19*(3), 807–837. https://doi.org/10.1002/2017GC007348

Clague, D. A., Caress, D. W., Paduan, J. B., & Le Saout, M. (2021). Interpreted outlines of lava flows, faults, and eruptive fissures as shapefiles for the distal South Rift Zone region of Axial Seamount, version as of July 2021. *Interdisciplinary Earth Data Alliance (IEDA)*. https://doi.org/10.26022/IEDA/330468

Clague, D. A., Dreyer, B. M., Paduan, J. B., Martin, J. F., Chadwick, W. W., Caress, D. W., et al. (2013). Geologic history of the summit of Axial Seamount, Juan de Fuca Ridge. *Geochemistry, Geophysics, Geosystems*, *14*(10), 4403–4443. https://doi.org/10.1002/ggge.20240

Clague, D. A., Paduan, J., Caress, D., Chadwick, W., Le Saout, M., Dreyer, B., & Portner, R. (2018a). Interpreted outlines (version 2) as shapefiles of the 2011 lava flows and eruptive fissures at Axial Seamount, Juan de Fuca Ridge (investigator David Clague). *Integrated Earth Data Applications (IEDA)*. https://doi.org/10.1594/IEDA/324415

Clague, D. A., Paduan, J., Caress, D., Chadwick, W., Le Saout, M., Dreyer, B., & Portner, R. (2018b). Interpreted outlines (version 2) as shapefiles of the 2015 lava flows and eruptive fissures at Axial Seamount, Juan de Fuca Ridge (investigator David Clague). *Integrated Earth Data Applications (IEDA)*. https://doi.org/10.1594/IEDA/324417

Cowen, J. P. P., Fornari, D. J. J., Shank, T. M. M., Love, B., Glazer, B. H., Treusch, A. H., et al. (2007). Volcanic eruptions at East Pacific Rise near 9° 50′ north. *Eos, Transactions American Geophysical Union*, *88*(7), 81–83. https://doi.org/10.1029/2007eo070001

Cowie, P. A., Scholz, C. H., Edwards, M., & Malinverno, A. (1993). Fault strain and seismic coupling on mid-ocean ridges. *Journal of Geophysical Research*, *98*(B10), 17911–17920. https://doi.org/10.1029/93jb01567

Demets, C., Gordon, R. G., & Argus, D. F. (2010). Geologically current plate motions. *Geophysical Journal International*, *181*(1), 1–80. https://doi.org/10.1111/j.1365-246X.2009.04491.x

DeMets, C., Gordon, R. G., Argus, D. F., & Stein, S. (1994). Effect of recent revisions to the geomagnetic reversal time scale on estimates of current plate motions. *Geophysical Research Letters*, *21*(20), 2191–2194. https://doi.org/10.1029/94GL02118

Deschamps, A., Grigné, C., Le Saout, M., Soule, S. A., Allemand, P., Van Vliet-Lanoe, B., & Floc'H, F. (2014). Morphology and dynamics of inflated subaqueous basaltic lava flows. *Geochemistry, Geophysics, Geosystems*, *15*(6), 2128–2150. https://doi.org/10.1002/2014GC005274

Detrick, R. S., Buhl, P., Vera, E., Mutter, J., Orcutt, J., Madsen, J., & Brocher, T. (1987). Multi-channel seismic imaging of a crustal magma chamber along the East Pacific Rise. *Nature*, *326*(5), 35–41. https://doi.org/10.1038/326035a0

Escartín, J., Cowie, P. A., Searle, R. C., Allerton, S., Mitchell, N. C., MacLeod, C. J., & Slootweg, A. P. (1999). Quantifying tectonic strain and magmatic accretion at a slow spreading ridge segment, Mid-Atlantic Ridge, 29°N. *Journal of Geophysical Research*, *104*(B5), 10421–10437. https://doi.org/10.1029/1998jb900097

Escartín, J., Soule, S. A., Fornari, D. J., Tivey, M. A., Schouten, H., & Perfit, M. R. (2007). Interplay between faults and lava flows in construction of the upper oceanic crust: The East Pacific Rise crest 9°25′-9°58′N. *Geochemistry, Geophysics, Geosystems*, *8*(6), Q06005. https://doi.org/10.1029/2006GC001399

Fornari, D. J., Shank, T., Von Damm, K. L., Gregg, T. K. P., Lilley, M., Levai, G., et al. (1998). Time-series temperature measurements at high-temperature hydrothermal vents, East Pacific Rise 9°49′-51′N: Evidence for monitoring a crustal cracking event. *Earth and Planetary Science Letters*, *160*(3–4), 419–431. https://doi.org/10.1016/S0012-821X(98)00101-0

Fornari, D. J., Tivey, M., Schouten, H., Perfit, M., Yoerge, D., Bradley, A., et al. (2004). Submarine lava flow emplacement at the east Pacific rise 9° 50′N: Implications for uppermost ocean crust stratigraphy and hydrothermal fluid circulation. *Geophysical Monograph Series*, *148*, 187–217. https://doi.org/10.1029/148GM08

Fornari, D. J., Von Damm, K. L., Bryce, J. G., Cowen, J. P., Ferrini, V., Fundis, A., et al. (2012). The East Pacific Rise between 9°N and 10°N: Twenty-five years of integrated, multidisciplinary oceanic spreading center studies. *Oceanography*, *25*(1), 18–43. https://doi.org/10.5670/oceanog.2012.02

Gibson, I. L. (1969). The structure and volcanic geology of an axial portion of the Main Ethiopian Rift. *Tectonophysics*, *8*(4–6), 561–565. https://doi.org/10.1016/0040-1951(69)90054-7

Gudmundsson, A. (1995). The geometry and growth of dykes. In R. Balkema (Ed.), *Physics and chemistry of dykes* (pp. 23–34).

Gudmundsson, A., & Bäckström, K. (1991). Structure and development of the Sveinagja graben, northeast Iceland. *Tectonophysics*, *200*(1–3), 111–125. https://doi.org/10.1016/0040-1951(91)90009-H

Han, S., Carbotte, S. M., Carton, H., Mutter, J. C., Aghaei, O., Nedimović, M. R., & Canales, J. P. (2014). Architecture of on- and off-axis magma bodies at EPR 9°37-40′N and implications for oceanic crustal accretion. *Earth and Planetary Science Letters*, *390*, 31–44. https://doi.org/10.1016/j.epsl.2013.12.040

Harding, A. J., Kent, G. M., & Orcutt, J. A. (1993). A multichannel seismic investigation of upper crustal structure at 9°N on the East Pacific Rise: Implications for crustal accretion. *Journal of Geophysical Research*, *98*(B8), 925–944. https://doi.org/10.1029/93jb00886

Harper, G. D. (1984). The Josephine ophiolite, northwestern California. *Geological Society of America Bulletin*, *95*(9), 1009–1026. https://doi.org/10.1130/0016-7606(1984)95<1009:tjonc>2.0.co;2

Haymon, R. M., Fornari, D. J., Edwards, M. H., Carbotte, S., Wright, D., & Macdonald, K. C. (1991). Hydrothermal vent distribution along the East Pacific Rise crest (9°09′-54′N) and its relationship to magmatic and tectonic processes on fast-spreading mid-ocean ridges. *Earth and Planetary Science Letters*, *104*(2–4), 513–534. https://doi.org/10.1016/0012-821X(91)90226-8

Haymon, R. M., Fornari, D. J., Von Damm, K. L., Lilley, M. D., Perfit, M. R., Edmond, J. M., et al. (1993). Volcanic eruption of the mid-ocean ridge along the East Pacific Rise crest at 9°45-52′N: Direct submersible observations of seafloor phenomena associated with an eruption event in April, 1991. *Earth and Planetary Science Letters*, *119*(1–2), 85–101. https://doi.org/10.1016/0012-821X(93)90008-W

Hjartardóttir, Á. R., Einarsson, P., & Björgvinsdóttir, S. G. (2016). Fissure swarms and fracture systems within the Western Volcanic Zone, Iceland—Effects of spreading rates. *Journal of Structural Geology*, *91*, 39–53. https://doi.org/10.1016/j.jsg.2016.08.007

Hjartardóttir, Á. R., Einarsson, P., Bramham, E., & Wright, T. J. (2012). The Krafla fissure swarm, Iceland, and its formation by rifting events. *Bulletin of Volcanology*, *74*(9), 2139–2153. https://doi.org/10.1007/s00445-012-0659-0

Hjartardóttir, A. R., Einarsson, P., Magnúsdóttir, S., Björnsdóttir, T., & Brandsdóttir, B. (2016). Fracture systems of the Northern Volcanic Rift Zone, Iceland: An onshore part of the Mid-Atlantic plate boundary. *Geological Society Special Publication*, *420*(1), 297–314. https://doi.org/10.1144/SP420.1

Hjartardóttir, Á. R., Einarsson, P., & Sigurdsson, H. (2009). The fissure swarm of the Askja volcanic system along the divergent plate boundary of N Iceland. *Bulletin of Volcanology*, *71*(9), 961–975. https://doi.org/10.1007/s00445-009-0282-x

Ito, G., & Behn, M. D. (2008). Magmatic and tectonic extension at mid-ocean ridges: 2. Origin of axial morphology. *Geochemistry, Geophysics, Geosystems*, *9*(9), Q09O12. https://doi.org/10.1029/2008GC001970

Kappel, E. S., & Ryan, W. B. F. (1986). Volcanic episodicity and a non-steady state rift valley along northeast Pacific spreading centers: Evidence from sea MARC I. *Journal of Geophysical Research*, *91*(B14), 13925. https://doi.org/10.1029/jb091ib14p13925

Karson, J. A. (2002). Geologic structure of the uppermost oceanic crust created at fast-to intermediate-rate spreading centers. *Annual Review of Earth and Planetary Sciences*, *30*(1), 347–384. https://doi.org/10.1146/annurev.earth.30.091201.141132

Karson, J. A., Kelley, D. S., Fornari, D. J., Perfit, M. R., & Shank, T. M. (2015). *Discovering the deep: A photographic atlas of the seafloor and oceanic crust*. Cambridge University Press. https://doi.org/10.1017/cbo9781139050524.010

Karson, J. A., Klein, E. M., Hurst, S. D., Lee, C. E., Rivizzigno, P. A., Curewitz, D., et al. (2002). Structure of uppermost fast-spread oceanic crust exposed at the Hess Deep Rift: Implications for subaxial processes at the East Pacific Rise. *Geochemistry, Geophysics, Geosystems*, *8*(1), 1002. https://doi.org/10.1029/2006gc001322

Koehn, D., Steiner, A., & Aanyu, K. (2019). Modelling of extension and dyking-induced collapse faults and fissures in rifts. *Journal of Structural Geology*, *118*, 21–31. https://doi.org/10.1016/j.jsg.2018.09.017

Le Saout, M., Clague, D. A., & Paduan, J. B. (2021). Faulting and magmatic accretion across the overlapping spreading center between Vance Segment and Axial South Rift, Juan de Fuca Ridge. *Geochemistry, Geophysics, Geosystems*, *23*, 1–12. https://doi.org/10.1029/2021gc010082

Le Saout, M., Thibaud, R., & Gente, P. (2018). Detailed analysis of near tectonic features along the East Pacific Rise at 16°N, near the mathematician hot spot. *Journal of Geophysical Research: Solid Earth*, *123*(6), 4478–4499. https://doi.org/10.1029/2017JB015301

Lister, J. R., & Kerr, R. C. (1991). Fluid-mechanical models of crack propagation and their application to magma transport in dykes. *Journal of Geophysical Research*, *96*(B6), 49–77. https://doi.org/10.1029/91jb00600

Lundgren, P., Poland, M., Miklius, A., Orr, T., Yun, S. H., Fielding, E., et al. (2013). Evolution of dike opening during the March 2011 Kamoamoa fissure eruption, Kīlauea Volcano, Hawai'i. *Journal of Geophysical Research: Solid Earth*, *118*(3), 897–914. https://doi.org/10.1002/jgrb.50108

Luyendyk, B. (1970). Origin and history of abyssal hills in the northeast Pacific Ocean. *Geological Society of America Bulletin*, *81*(8), 2237–2260. https://doi.org/10.1130/0016-7606(1970)81[2237:oahoah]2.0.co;2

Macdonald, K. C., & Fox, P. J. (1988). The axial summit graben and cross-sectional shape of the East Pacific Rise as indicators of axial magma chambers and recent volcanic eruptions. *Earth and Planetary Science Letters*, *88*(1–2), 119–131. https://doi.org/10.1016/0012-821X(88)90051-9

Macdonald, K. C., Fox, P. J., Alexander, R. T., Pockalny, R., & Gente, P. (1996). Volcanic growth faults and the origin of Pacific abyssal hills. *Nature*, *380*(6570), 125–129. https://doi.org/10.1038/380125a0

Macdonald, K. C., Fox, P. J., Miller, S., Carbotte, S., Edwards, M. H., Eisen, M., et al. (1992). The East Pacific Rise and its flanks 8-18°N: History of segmentation, propagation and spreading direction based on SeaMARC II and Sea Beam studies. *Marine Geophysical Researches*, *14*(4), 299–344. https://doi.org/10.1007/BF01203621

Marjanović, M., Barreyre, T., Fontaine, F. J., & Escartín, J. (2019). Investigating fine-scale permeability structure and its control on hydrothermal activity along a fast-spreading ridge (the East Pacific Rise, 9°43′-53′N) using seismic velocity, poroelastic response, and numerical modeling. *Geophysical Research Letters*, *46*(21), 0–2. https://doi.org/10.1029/2019gl084040

Marjanović, M., Carbotte, S. M., Carton, H., Nedimović, M. R., Mutter, J. C., & Canales, J. P. (2014). A multi-sill magma plumbing system beneath the axis of the East Pacific Rise. *Nature Geoscience*, *7*(11), 825–829. https://doi.org/10.1038/ngeo2272

Marjanović, M., Carbotte, S. M., Carton, H. D., Nedimović, M. R., Canales, J. P., & Mutter, J. C. (2018). Crustal magmatic system beneath the East Pacific Rise (8°20′ to 10°10′N): Implications for tectonomagmatic segmentation and crustal melt transport at fast-spreading ridges. *Geochemistry, Geophysics, Geosystems*, *19*(11), 4584–4611. https://doi.org/10.1029/2018GC007590

Mastin, L. G., & Pollard, D. D. (1988). Surface deformation and shallow dike intrusion processes at Inyo craters, Long Valley, California. *Journal of Geophysical Research*, *93*(B11), 13221–13235. https://doi.org/10.1029/jb093ib11p13221
McClinton, T., White, S. M., Colman, A., & Sinton, J. M. (2013). Reconstructing lava flow emplacement processes at the hot spot-affected Galápagos Spreading Center, 95°W and 92°W. *Geochemistry, Geophysics, Geosystems*, *14*(8), 2731–2756. https://doi.org/10.1002/ggge.20157
Mériaux, C. A., May, D. A., & Jaupart, C. (2022). The impact of vent geometry on the growth of lava domes. *Geophysical Journal International*, *229*(3), 1680–1694. https://doi.org/10.1093/gji/ggac005
Mutter, J. C., Barth, G. A., Buhl, P., Detrick, R. S., Orcutt, J. A., & Harding, A. J. (1988). Magma distribution across ridge-axis discontinuities on the East Pacific Rise from multichannel seismic images. *Nature*, *336*(6195), 156–158. https://doi.org/10.1038/336156a0
Nakamura, K. (1970). En echelon features of Icelandic ground fissures. *Acta Naturalia Islandica*, *2*(8), 1–15.
Neal, C. A., Brantley, S. R., Antolik, L., Babb, J. L., Burgess, M., Calles, K., et al. (2019). The 2018 rift eruption and summit collapse of Kīlauea Volcano. *Science*, *363*, 367–374. https://doi.org/10.1126/science.aav7046
Nur, A. (1982). The origin of tensile fracture lineaments. *Journal of Structural Geology*, *4*(1), 31–40. https://doi.org/10.1016/0191-8141(82)90004-9
Olive, J. A., & Dublanchet, P. (2020). Controls on the magmatic fraction of extension at mid-ocean ridges. *Earth and Planetary Science Letters*, *549*, 116541. https://doi.org/10.1016/j.epsl.2020.116541
Orcutt, J. A., Kennett, B. L. N., & Dorman, L. R. M. (1976). Structure of the East Pacific Rise from an ocean bottom seismometer survey. *Geophysical Journal of the Royal Astronomical Society*, *45*(2), 305–320. https://doi.org/10.1111/j.1365-246X.1976.tb00328.x
Rubin, A. M. (1990). A comparison of rift-zone tectonics in Iceland and Hawaii. *Bulletin of Volcanology*, *52*(4), 302–319. https://doi.org/10.1007/BF00304101
Rubin, A. M. (1992). Dike-induced faulting and graben subsidence in volcanic rift zones. *Journal of Geophysical Research*, *97*(B2), 1839–1858. https://doi.org/10.1029/91JB02170
Rubin, A. M., & Pollard, D. D. (1988). Dike-induced faulting in rift zones of Iceland and Afar. *Geology*, *16*(5), 413–417. https://doi.org/10.1130/0091-7613(1988)016<0413:DIFIRZ>2.3.CO;2
Ruch, J., Wang, T., Xu, W., Hensch, M., & Jónsson, S. (2016). Oblique rift opening revealed by reoccurring magma injection in central Iceland. *Nature Communications*, *7*, 1–7. https://doi.org/10.1038/ncomms12352
Self, S., Thordarson, T., Keszthelyi, L., Walker, G. P. L., Hon, K., Murphy, M. T., et al. (1996). Inflated pahoehoe lava flow fields. *American Geophysical Union*, *23*(19), 2689–2692. https://doi.org/10.1029/96gl02450
Sherrod, B. D. R., Sinton, J. M., Watkins, S. E., & Brunt, K. M. (2007). Geologic map of the state of Hawai'i. USGS Open File Report, (2007–1089).
Sinton, J., Bergmanis, E., Rubin, K. H., Batiza, R., Gregg, T. K. P., Gronvold, K., et al. (2002). Volcanic eruptions on mid-ocean ridges: New evidence from the superfast spreading East Pacific Rise, 17°–19°S. *Journal of Geophysical Research*, *107*(B6), 2115. https://doi.org/10.1029/2000jb000090
Soule, S. A., Fornari, D. J., Perfit, M. R., & Rubin, K. H. (2007). New insights into mid-ocean ridge volcanic processes from the 2005-2006 eruption of the East Pacific Rise, 9°46′N-9°56′N. *Geology*, *35*(12), 1079–1082. https://doi.org/10.1130/G23924A.1
Tentler, T., & Temperley, S. (2007). Magmatic fissures and their systems in Iceland: A tectonomagmatic model. *Tectonics*, *26*(5), 1–17. https://doi.org/10.1029/2006TC002037
Tolstoy, M., Cowen, J. P., Baker, E. T., Fornari, D. J., Rubin, K. H., Shank, T. M., et al. (2006). A sea-floor spreading event captured by seismometers. *Science*, *314*(5807), 1920–1922. https://doi.org/10.1126/science.1133950
Tolstoy, M., Waldhauser, F., Bohnenstiehl, D. R., Weekly, R. T., & Kim, W. Y. (2008). Seismic identification of along-axis hydrothermal flow on the East Pacific Rise. *Nature*, *451*(7175), 181–184. https://doi.org/10.1038/nature06424
Valentine, G. A., & Perry, F. V. (2006). Decreasing magma tic footprints of individual volcanoes in a waning basaltic field. *Geophysical Research Letters*, *33*(14), 2–6. https://doi.org/10.1029/2006GL026743
Wadsworth, F. B., Kennedy, B. M., Branney, M. J., von Aulock, F. W., Lavallée, Y., & Menendez, A. (2015). Exhumed conduit records magma ascent and drain-back during a Strombolian eruption at Tongariro volcano, New Zealand. *Bulletin of Volcanology*, *77*(9), 71. https://doi.org/10.1007/s00445-015-0962-7
Waldhauser, F., & Tolstoy, M. (2012). Seismogenic structure and processes associated with magma inflation and hydrothermal circulation beneath the East Pacific Rise at 9°50'N. *Geochemistry, Geophysics, Geosystems*, *12*(9), Q08T10. https://doi.org/10.1029/2011GC003568
Weiland, C. M., & Macdonald, K. C. (1996). Geophysical study of the East Pacific rise 15°N-17°N: An unusually robust segment. *Journal of Geophysical Research*, *101*(9), 20257–20273. https://doi.org/10.1029/96jb01756
Wessel, P., Luis, J. F., Uieda, L., Scharroo, R., Wobbe, F., Smith, W. H. F., & Tian, D. (2019). The generic mapping Tools version 6. *Geochemistry, Geophysics, Geosystems*, *20*(11), 5556–5564. https://doi.org/10.1029/2019GC008515
White, S. M., Haymon, R. M., & Carbotte, S. (2006). A new view of ridge segmentation and near-axis volcanism at the East Pacific Rise, 8°-12°N, from EM300 multibeam bathymetry. *Geochemistry, Geophysics, Geosystems*, *7*(12), Q12O05. https://doi.org/10.1029/2006GC001407
Wright, D. J. (2002). Crustal fissuring on the crest of the southern East Pacific Rise at 17°15′–40′S. *Journal of Geophysical Research*, *107*(B5), 2104. https://doi.org/10.1029/2001jb000544
Wright, D. J., Haymon, R. M., & Fornari, D. J. (1995). Crustal fissuring and its relationship to magmatic and hydrothermal processes on the East Pacific Rise crest (9°12′ to 54′N). *Journal of Geophysical Research*, *100*(B4), 6097–6120. https://doi.org/10.1029/94JB02876
Wright, D. J., Haymon, R. M., & MacDonald, K. C. (1995). Breaking new ground: Estimates of crack depth along the axial zone of the East Pacific Rise (9°12′-54′N). *Earth and Planetary Science Letters*, *134*(3–4), 441–457. https://doi.org/10.1016/0012-821X(95)00081-M
Wright, T. J., Ebinger, C., Biggs, J., Ayele, A., Yirgu, G., Keir, D., & Stork, A. (2006). Magma-maintained rift segmentation at continental rupture in the 2005 Afar dyking episode. *Nature*, *442*(7100), 291–294. https://doi.org/10.1038/nature04978
Wright, T. J., Sigmundsson, F., Pagli, C., Belachew, M., Hamling, I. J., Brandsdóttir, B., et al. (2012). Geophysical constraints on the dynamics of spreading centres from rifting episodes on land. *Nature Geoscience*, *5*(4), 242–250. https://doi.org/10.1038/ngeo1428
Wu, J., Parnell-Turner, R., Fornari, D. J., Kurras, G., Berrios-Rivera, N., Barreyre, T., & McDermott, J. M. (2022). Extent and volume of lava flows erupted at 9°50′N, East Pacific Rise in 2005–2006 from autonomous underwater vehicle surveys. *Geochemistry, Geophysics, Geosystems*, *23*(3), 1–19. https://doi.org/10.1029/2021gc010213
Xu, M., Canales, J. P., Carbotte, S. M., Carton, H., Nedimović, M. R., & Mutter, J. C. (2014). Variations in axial magma lens properties along the East Pacific Rise (9°30′N–10°00′N) from swath 3-D seismic imaging and 1-D waveform inversion. *Journal of Geophysical Research: Solid Earth*, *119*(4), 2721–2744. https://doi.org/10.1002/2013JB010730.Received
Yoerger, D. R., Bradley, A. M., Walden, B. B., Singh, H., & Bachmaver, R. (1998). Surveying a subsea lava flow using the Autonomous Benthic Explorer (ABE). *International Journal of Systems Science*, *29*(10), 1031–1044. https://doi.org/10.1080/00207729808929596
Yoerger, D. R., Jakuba, M., Bradley, A. M., & Bingham, B. (2007). Techniques for deep sea near bottom survey using an autonomous underwater vehicle. *The International Journal of Robotics Research*, *26*(1), 41–54. https://doi.org/10.1177/0278364907073773